Chapter 5
Iron Mineralogy, Secondary Overprints, and Paleoredox Conditions During Deposition of the Mid-Proterozoic Belt Supergroup

Coauthors:

Samuel M. Webb, Joseph L. Kirschvink, and Woodward W. Fischer

5.1 Abstract

Observing iron chemistry in sedimentary rocks is one of the primary methods for understanding ancient redox environments; however, major questions still revolve around Proterozoic redox chemistry after the rise of oxygen. We utilize a hybrid approach coupling microscale textural techniques of light microscopy, electron microscopy, magnetic microscopy, and (synchrotron) x-ray spectroscopy with bulk rock magnetic techniques to untangle complex iron mineralogy in a case study of the ~1.4 Ga lower Belt group, Belt Supergroup, Montana and Idaho. Samples were collected across a range of metamorphic, metasomatic, and diagenetic regimes to understand post-depositional iron transformation. A pyrrhotite-siderite isograd was identified marking metamorphic iron-bearing mineral reactions beginning in the sub-greenschist facies samples. Even in the best-preserved parts of the Belt Basin, secondary overprints were common including recrystallization of iron sulfide phases, base metal sulfides, and nano-phase pyrrhotite. Despite these overprints, some record of redox chemistry was preserved in the early diagenetic framboidal pyrite and detrital iron oxides including (sub)micron-sized magnetite. Although only a small percentage of the samples (<10 ppm), this magnetite represents an important supply of highly-reactive iron to the basin for the formation of pyrite. Based on our analyses, we interpret the Belt Basin as having shallow oxic waters overlying sediments with anoxic and sulfidic pore fluids, potentially with suboxic or euxinic deep waters, consistent with the redox results from some earlier studies and evidence for eukaryotes.

5.2 Introduction

Understanding the early Earth's atmospheric and oceanic chemistry has important implications for understanding the evolution of life. Specifically, paleoredox during the Proterozoic is vital to understanding the emergence of eukaryotes and multicellular life since both depend on oxygen for biosynthesis

and for metabolic processes (Embley and Martin, 2006; Summons et al., 2006). Almost all eukaryotes today contain mitochondria, which are also believed to be in the last common eukaryotic ancestor (Embley and Martin, 2006), and the mitochondrial aerobic respiration pathway requires oxic environments with approximately 0.01 present atmospheric oxygen levels before organisms are forced to utilize other metabolisms such as fermentation or die (Berkner and Mashall, 1964; Fischer, 2016).

Observations of iron chemistry and mineralogy in sedimentary rocks have been utilized for decades to understand ancient environmental redox shifts, primarily due to iron's redox sensitivity as it cycles between +II and +III valence states (e.g. Cloud, 1968; Holland, 1984). One popular method of measuring iron and iron redox in rock samples is iron speciation, a bulk sequential chemical extraction technique measuring the proportions of different reactive iron species, which are mapped to redox conditions based on empirical calibrations from modern sediment samples (Poulton and Canfield, 2005, 2011). Iron speciation gives surprising results that have dramatically altered views on Proterozoic geochemistry, revealing a complex picture of predominately anoxic iron-rich (i.e. ferruginous) conditions with additional oxic and anoxic H2S-rich (i.e. euxinic) environments varying in time, geography, and water depth (e.g. Gilleaudeau and Kah, 2015; Kendall et al., 2009; Planavsky et al., 2011; Shen et al., 2003; Sperling et al., 2014). However, it is poorly understood how post-depositional processes such as diagenesis, metamorphism and metasomatism could affect these proxies in the sedimentary rock record (e.g. Clarkson et al., 2014; Reinhard et al., 2013). We chose an alternative approach that allows us to analyze the redox state of iron within samples while also preserving textural data to understand how and when the iron-bearing minerals formed. In order to test the application of novel techniques to understand the iron mineralogy, post-depositional alteration, and paleoredox, we chose a location with well-known metamorphic gradients, the classic mid-Proterozoic basin of the Belt Supergroup.

5.3 Geology of the Belt Supergroup

The Belt Supergroup, dated between 1470 Ma and 1401 Ma (Anderson and Davis, 1995; Evans et al., 2000; Sears et al., 1998), is an extensive, well-preserved, mid-Proterozoic sedimentary succession, currently exposed across parts of Montana, Idaho, Washington, Alberta, and British Columbia (Fig. 5.1). Over 18 km thick stratigraphically in some regions (Winston and Link, 1993), the Belt Supergroup contains a mixture of siliciclastic and carbonate rocks (Fig. 5.2), deposited in a large intercontinental lake (e.g. Grotzinger, 1981; Winston, 1986) or a (restricted) marine setting (e.g. Cressman, 1989; Luepke and Lyons, 2001; Lyons et al., 2000). Paleontologically, the strata preserve an abundance of stromatolites and diverse micro- and macrofossils, some of which are interpreted to be eukaryotes (e.g. Horodyski et al., 1989; Knoll et al., 2006). Due to increased thickness to the west (burial metamorphism) and intrusions in the west of syndepositional sills and Cretaceous batholiths, metamorphic conditions range from sub-biotite facies in Glacier National Park and the Helena Embayment to garnet facies by Lake Pend Orielle to staurolite facies near batholiths in Idaho (Duke and Lewis, 2010) (Fig. 5.1).

We focus on the green, grey, and black shales, siltstones, and sandstones of the lower Belt group (Fig. 5.2, Fig. S5.1), which have been previously studied to understand redox conditions of mid-Proterozoic time. Based on sulfate levels, sulfur isotopes, nitrogen isotopes, and organic-carbon richness as well as basin-wide laminations reminiscent of the Black Sea, many previous studies on the Prichard, Newland, and Greyson Formations suggested a stratified euxinic basin with oxic surface waters (Gellatly and Lyons, 2005; Huebschman, 1973; Luepke and Lyons, 2001; Lyons et al., 2000; Stüeken, 2013). Additional support for euxinic bottom water conditions comes syndepositional to early diagenetic sulfide-hosted base metal deposits in the lower Belt group, notably the Pb-Zn-Ag Sullivan Deposit in British Columbia and the Cu-Co-Ag Black Butte Deposit in

the Helena Embayment (Graham et al., 2012; Hamilton et al., 1982; Present et al., in review). However, contrary to these proxies, iron speciation results from the Newland Formation suggested predominantly ferruginous water column conditions with episodic euxinic events (Planavsky et al., 2011). Our study sheds light on this geochemical result, highlights important caveats in interpreting iron speciation results, and deconvolves complex iron mineralogy to make paleoredox interpretations.

5.4 Coupled Textural and Bulk Methods

When investigating rocks that have undergone diagenesis and metamorphism, it is necessary to observe samples at a microscale to connect chemistry and mineralogy with petrographic textures within the rocks and to ordinate mineralization using cross-cutting relationships. First, samples were made into thin or thick sections and studied using transmitted and reflected optical microscopy. Further petrographic observations were made in the Caltech GPS Division Analytical Facility using the Zeiss 1550VP Field Emission scanning electron microscope with a Robinson-type backscatter electron detector for imaging. This instrument contains a paired Oxford X-Max SDD X-ray Energy Dispersive Spectrometer (EDS) system used to determine X-ray spectra of elemental abundance and HKL Electron Back Scatter Diffraction (EBSD) system used to determine structural information. Quantitative chemical information for formula derivation was determined using a JXA-8200 Electron Probe Micro-Analyzer (EPMA).

In addition to these more conventional textural analyses, we used Caltech's ultrahigh resolution scanning SQuID microscope (UHRSSM) to create 2D images of the magnetic field (sensitivity of 0.1 nT) at a resolution of 40 to 130 μm after giving samples a saturation magnetization in order to identify ferromagnetic minerals texturally. We also performed synchrotron-based X-ray spectroscopy at the Stanford Synchrotron Radiation Lightsource. High energy X-

ray fluorescence (XRF) imaging was performed on thin and thick sections using energies from 20,200 eV to 10,000 eV at beam line 10-2 to characterize elemental abundances including trace metals over large regions in 30-35 μm pixels. Standards for quantification were run at each beam time session with the same collection parameters. Synchrotron-based X-ray absorption near-edge spectroscopy (XANES/XAS) was paired with XRF and elemental imaging using beam lines 14-3 and 2-3 at energies centering around the sulfur absorption edge (2472 eV) and the iron absorption edge (7112 eV) respectively. XANES was performed in fluorescence mode at specific 2-4 μm-sized spots to determine the chemical form of elements (oxidation state, orbital electronics, type and number of neighbors). Differences in the shape and K-edge of these absorption spectra can distinguish between a wide range of Fe- and S- bearing minerals (Fleet, 2005; O'Day et al., 2004). Additionally, XRF maps were collected at multiple excitation energies over the XANES spectrum, and images differentiating between phases, coordination environment and redox state were created by fitting the endmember spectra of different minerals from the sample to the XRF maps (e.g. Mayhew et al., 2011). XRF elemental maps were processed using the MicroAnalysis Toolkit (Webb, 2011) and XAS data was processed using SIXPACK (Webb, 2005).

On the same sample used for textural analyses and/or on a neighboring specimen, non-destructive bulk rock magnetic experiments were performed to observe fundamental magnetic properties that can distinguish between different magnetic minerals (e.g. Peters and Dekkers, 2003). Rock magnetic experiments were performed on all samples at the Caltech Paleomagnetics Laboratory using a 2G Enterprises SQuID magnetometer following the RAPID protocols, and analyzed using the RAPID Matlab scripts (Kirschvink et al., 2008). Our protocol includes measurements of alternating field (AF) demagnetization of the natural remanent magnetization (NRM), rotational remanent magnetization (RRM) acquisition and demagnetization, anhysteretic remanent magnetization (ARM)

acquisition and demagnetization, isothermal remanent magnetization (IRM) acquisition and demagnetization, and backfield IRM acquisition. At the Institute for Rock Magnetism at the University of Minnesota, hysteresis loops and backfield acquisition measurements were also measured on all specimens at room temperature using a Princeton Measurements Vibrating Sample Magnetometer in order to characterize mineralogy, grain size, and magnetite abundance. Using the Quantum Designs Magnetic Property Measurement System (MPMS) at the Institute for Rock Magnetism, samples were cooled to 10 K under a variety of applied fields to confirm the presence of ferromagnetic minerals using unique low temperature transitions.

A total of 63 samples were analyzed using these coupled textural and bulk methods from all units of the lower Belt Supergroup (except the carbonate Altyn Formation) and the overlying red and green siliciclastic units of the lower Ravalli Group, spanning a range of metamorphic grades and paleo-water depths; additional description and GPS information can be found in Table S5.1, Slotznick et al. (2015), and Slotznick et al. (2016). Mineralogical results are summarized in Figure 5.1 with additional minerals listed in Table S5.2 and detailed data in Figures S5.2-S5.5.

5.5 Metamorphic Transformations and Diagenetic Overprints

By looking at correlated strata across a metamorphic gradient, we were able to demarcate a new iron-mineral isograd as well note other changes to iron-bearing minerals that occurred through progressive diagenesis/metamorphism. Recognized in both Glacier National Park (Slotznick et al., 2016) and in the Helena Embayment, pyrrhotite and siderite appear only in rocks in the western halves of these sub-basins, which we interpret as secondary overprints created by increased burial metamorphism (Fig. 5.1). Mineralogical variations based on outcropping of distinct stratigraphic units was controlled for by sampling stratigraphically correlated members of the Appekunny Formation across Glacier

National Park (Slotznick et al., 2016) and focusing on the lower Newland Formation across the Helena Embayment. Pyrrhotite can form from the metamorphic transformation of pyrite and addition of iron from neighboring iron-bearing minerals or from externally supplied iron-rich fluids; this reaction can begin at 200°C in the presence of organic matter or a reducing environment, with some experiments indicating transformation at even lower temperatures (Craig and Vokes, 1993; Hall, 1986; Moreau et al., 2005; Raub et al., 2012). Although pyrrhotite can be detrital or diagenetic in origin (Horng and Roberts, 2006; Larrasoaña et al., 2007), there is abundant pyrite, but no pyrrhotite in the Appekunny Formation on the east side of Glacier National Park and in the lower Belt units near White Sulphur Springs and the Black Butte Deposit, supporting our interpretation of a metamorphic isograd. Similarly, siderite as identified magnetically using RRM (Fig. S5.2) and its low temperature transition on the MPMS (Fig. S5.3), is only found in samples in the western halves of Glacier National Park and the Helena Embayment, while Fe-rich dolomite was identified chemically using EDS and EPMA across these sub-basins (Tables S5.2, S5.3). We believe that small domains of siderite formed as iron was repartitioned in these Fe-rich carbonates or was added from iron silicates, iron sulfides, or iron-rich fluids during burial metamorphism (e.g. French, 1973; Kholodov and Butuzova, 2008; Piché and Jébrak, 2006).

The pyrrhotite-siderite isograd occurs well below the biotite zone highlighting that these iron mineral reactions are occurring in rocks of very low metamorphic grade, often in rocks not considered “metamorphosed”. Both of these metamorphic reactions can utilize iron from within the pyrite, highly reactive iron, and silicate iron pools in a closed system or from external sources in an open system. Recent iron speciation studies often screen for pyrrhotite using hydrochloric acid extractions for acid-volatile sulfides (e.g. Asael et al., 2013; Li et al., 2015; Planavsky et al., 2011) and most methodologies have a separate carbonate extraction step, but if there is no petrography or investigation of iron

source for these secondary minerals (e.g. Partin et al., 2015), interpretation of iron speciation studies can be difficult.

Pyrrhotite and siderite continue to be found through the biotite zone/greenschist facies rocks further west in the Belt Basin. Additional minerals suggest further transformations within the iron system, specifically the presence of an iron calcium aluminosilicate (epidote probably or pumpellyite) and an iron titanium oxide with trace Mn (ilmenite or titanomagnetite) (Table S5.2, Fig. 5.3C). Epidote and pumpellyite are common silicate metamorphic minerals of lower greenschist and prehnite-pumpellyite facies. Prior studies on regional metamorphic gradients do not discuss the presence of pumpellyite and classify the region as greenschist facies (Duke and Lewis, 2010 and references therein); epidote has been previously identified within the garnet zone (Cressman, 1989). Pumpellyite and epidote are proposed to form from reactions involving calcium aluminosilicates, muscovite, chlorite, carbonate, and/or Fe-rich external fluids (Bishop, 1972; Muffler and White, 1969). A reaction pathway utilizing carbonate is supported by the disappearance of the (large) Fe-rich dolomite grains, identified texturally in samples from Glacier National Park and the Helena Embayment. Biotite, ubiquitous through the Prichard Fm. (Table S5.2, S5.3) (Cressman, 1989), is also believed to form through the reaction of muscovite, chlorite, carbonates, iron oxides, iron sulfides, and/or fluids (Ferry, 1983, 1984, 2007). The iron titanium oxide with trace amounts of Mn likely formed from recrystallization of titanium oxides with other iron-bearing minerals or iron-rich fluids (Ferry, 1988); titanium oxides, identified using EDS, are common throughout the Glacier National Park and Helena Embayment regions, but become rarer to the west (Table S5.2). These metamorphic reactions highlight the mobility of iron in the greenschist facies; iron moves between the highly-reactive and silicate iron pools and possible external fluids can transport iron in an open system.

Quantitative analysis of our textural XRF maps highlights that there are similar amounts of iron and base metals across the Belt Basin with slight

variations based on lithology and region, suggesting either similar initial provenance and redox chemistries or a wide-spread homogenization in post-depositional metamorphic events (Table S5.4). Although greater variance and higher trace metal abundances are seen in our data than prior work, previous bulk XRF and ICP-MS studies also suggested pervasive diagenetic basinal brines across the sub-biotite zone (González-Álvarez and Kerrich, 2010; González-Álvarez et al., 2006). Striking differences are only observed in Fe-Cu-As-Pb abundance within the massive sulfide zones of the Black Butte Deposit. Textural high-energy XRF maps (Figs. S5.6-S5.9) paired with S XANES and EDS-SEM images highlight that the plentiful base-metals identified throughout the lower Belt are usually mineralized as sulfides (Table S5.2). Even in the best preserved parts of the Belt Supergroup, the east side of Glacier National Park and the Helena Embayment far from the ore-containing sulfide zones, there are Cu, Pb, Zn, and Ag sulfides, highlighting the mobility of these metals as well as sulfur in secondary diagenetic recrystallization events probably involving diagenetic/metasomatic fluids in an open system (e.g. González-Álvarez and Kerrich, 2010; González-Álvarez et al., 2006). Sometimes base-metal sulfides occur as separate grains (Figs. S5.10, S5.15), but often there are multiple sulfide phases within the same nodule (Figs. 5.4, S5.12-S5.14), emphasizing that recrystallization of original iron minerals occurred to incorporate trace metals. MPMS experiments also identified nano-phase pyrrhotite, i.e. pyrrhotite below the micron-size-threshold for ferromagnetism, in most specimens that did not contain ferromagnetic pyrrhotite throughout the lower Belt (Figs. 5.5A, S5.3). This fine-grained pyrrhotite can form at temperatures of 85-95°C (Aubourg and Pozzi, 2010). Although the amount of nano-phase pyrrhotite cannot be quantified using our methods, its presence suggests that the pyrite-pyrrhotite metamorphic transformation had begun even east of the pyrrhotite-siderite gradient described above, probably in small domains within pyrite. The movement of iron from

pyrite to any other phase or out of the system entirely will affect iron speciation proxies and make interpretations for paleoredox difficult.

Chlorite and calcite rims seen around trace-metal-bearing pyrrhotite and pyrite nodules in samples on the west side of Glacier National Park (Figs. 5.3D, 5.4) highlight an additional redox-transforming reaction moving iron from sulfides to silicates; therefore, more than one recrystallization event affected these slightly higher-grade rocks, which are still sub-biotite zone. Based on our textural analyses, we found that recrystallization is present across the entire Belt Basin, and most of the pyrite occurs in large euhedral grains cross-cutting fine-grained matrix minerals (e.g. Figs. S5.12, S5.17). However, there is a notable increase in grain size to the west, observable in both the matrix minerals and in the iron sulfides and oxides (compare Figs. 5.3ABEF, S5.10-S5.12 to Figs. 5.3D, 5.4, S5.13-S5.15 to Figs. 5.3AC, S5.16-S5.18). Coercivity spectra of the ferromagnetic minerals spanning the extent of the lower Belt Supergroup also highlight the recrystallization of magnetite into other minerals (Fig. S5.2); although conservatively, some of this change could be due to an increase in the proportion of other magnetic minerals. Previous work has suggested the formation of magnetite in the biotite zone based on petrography and trace element work of the Ravalli Group (Nadoll et al., 2012), and our sample from the Burke Formation also contains large multi-domain magnetite identified magnetically (Fig. 5.5B) and large euhedral (secondary) iron oxides up to 270 um identified petrographically. The coercivity spectrum of our Burke formation sample suggests two size populations of magnetite (Fig. S5.2) and the Fuller Test for nature of magnetization, which has only been calibrated for predominantly magnetite-bearing samples, suggests some of this magnetite is detrital due to the weak NRM:IRM ratio of 1:1000 (Fig. 5.5C) (Fuller et al., 1988; Fuller et al., 2002). For magnetite in the most westward sample of the Prichard Formation, the Fuller test suggests the magnetization carried is a chemical remanent magnetization (NRM:IRM ratio of 1:10) from recrystallization and/or

precipitation of new magnetite (Fig. 5.5C). In these greenschist facies rocks, recrystallization events and metamorphic transformations have overprinted the primary record of iron-oxides and iron-sulfides as well as iron-silicates and carbonates in multiple events that may be impossible to separate. Studying the iron mineralogy of the lower Belt Supergroup both texturally and magnetically reveals the involvement of iron-bearing minerals in metamorphic and diagenetic alterations in an open system, which need to be peeled away to discover the primary mineralogy and paleoredox; a task that is simplified by focusing on the least-altered regions of the Belt Basin.

5.6 Primary Mineralogy and Paleoredox

One of the more surprising results of our mineralogical studies was the ubiquitous presence of magnetite in all samples from the lower Belt (other than the red Appekunny Member 1). We double checked initial findings from coercivity spectra (Fig. S5.2; Slotznick et al., 2016; Slotznick et al., 2015) using hysteresis loops and MPMS to confirm magnetite's presence in both well-preserved rocks as well as in samples from the sulfide zones of the Black Butte Deposit and western greenschist facies (Figs. 5.5A, S5.3, S5.4). In many samples from the east side of Glacier National Park and White Sulphur Springs regions, magnetite is the only ferromagnetic mineral. The Day Plot of these samples suggests that the grain size for much of magnetite is between 0.1 to 20 μm (pseudo-single domain) (Fig. 5.5B) (Day et al., 1977; Dunlop, 2002). The Fuller Test suggests the magnetite in the White Sulphur Springs and Glacier National Park regions is by and large detrital in origin, due to the NRM:IRM ratios of 1:1000 (Fig. 5.5C). We therefore interpret the magnetite as a highly-reactive iron residue remaining after scavenging by early diagenetic sulfides.

Magnetite abundance, calculated by comparing the saturation magnetization with that of magnetite (Klein et al., 2014), in all lower Belt samples is approximately 1-8 ppm with 1.2 wt% magnetite in the Burke Formation sample

(Table S5.5). We were unable to image the magnetite using the SEM due to its low-abundance. Notably, our magnetite abundance calculations are much lower than those determined by chemical extraction. Even once correcting by the stoichiometry of magnetite, our results are one order of magnitude lower than the 0.06 to 0.17 wt% extracted iron from magnetite from disseminated pyritic drill core shales of the Black Butte Deposit and another order of magnitude below 0.10 to 0.51 wt% iron from magnetite in the disseminated pyritic and sulfide zone drill core shales of the Soap Gulch Prospect (Lyons et al., 2000; Planavsky et al., 2011). Two explanations exist for this disparity: 1) The high ratio of paramagnetic minerals such as chlorite and illite to magnetite within the samples made hysteresis corrections and precise determination of saturation magnetization difficult (Fig. S5.4), which could also explain why calculated magnetite percentages show such a tight range, or 2) iron sequential extraction by ammonium oxalate (after sodium acetate and dithionite extractions) dissolved other minerals such as iron carbonates in addition to magnetite within the sample (e.g. Algoe et al., 2012; Raiswell et al., 2011; Reinhard et al., 2009).

Understanding this difference is important due to the relative amount of iron attributed to magnetite using iron speciation; in the Newland Formation samples, the iron from the ammonium oxalate extraction accounts 2 to 10% of the total iron in the Black Butte Deposit and 6 to 21% of the total iron in Soap Gulch samples. The high percentage of iron from the ammonium oxalate extraction, especially for Soap Gulch samples, is an important contributor to the iron speciation data implying ferruginous paleoredox for the Newland Formation. The Soap Gulch prospect is to the west of the pyrrhotite-siderite isograd, and both siderite and pyrrhotite, targeted for extraction in the sodium acetate extraction for carbonates (Poulton and Canfield, 2005; Reuschel et al., 2012), may not completely dissolve and then are sequentially extracted with magnetite (Burton et al., 2006; Raiswell et al., 2011; Reinhard et al., 2009). While all samples from both cores were tested to have < 0.1 wt% pyrrhotite (Planavsky et al., 2011), we

are discussing percentages at the limits of chemical extraction so this amount could be important. Therefore the ferruginous iron speciation result in the Soap Gulch samples may come from issues with the sequential extraction technique and unrecognized metamorphic overprints moving iron from the pyrite or silicate pool toward the highly-reactive pool.

The main contributor for a ferruginous paleoredox interpretation from iron speciation of the Black Butte Deposit shales and an important factor for the Soap Gulch Prospect shales is the presence of iron carbonates. The Black Butte Deposit samples had a high percentage of iron extracted in the sodium acetate step (the carbonate pool) accounting for between 2 to 4% and 12 to 25% of the total iron in respectively pyrite-rich and pyrite-poor samples of the Black Butte Deposit and 2 to 16% of the total iron in Soap Gulch samples (Planavsky et al., 2011). Our study did find Fe-bearing dolomite within the Newland Formation and the Appekunny Formation in addition to the magnetic siderite in western samples (Tables S5.2, S5.3), but textural imaging of these carbonates suggests they are cements or secondary diagenetic transformations with clear zonation (Figs. 5.3D-F). Therefore, we interpret the Fe-bearing carbonates in the best preserved lower Belt samples as indicative of anoxic pore-water processes, not water column redox conditions.

Pyrite is present in almost all of the sampled lower Belt rocks, although it is often recrystallized as described above (Table S5.2). However, in the best-preserved rocks of the Appekunny and Newland Formations, there are examples of small aggregates of euhedral pyrite grains similar to the pyrite framboids observed in modern anoxic and sulfidic waters and sediments (Figs. 5.3ABF, S5.19E) (Wilkin and Barnes, 1997; Wilkin et al., 1996). Based on hydrodynamic calculations of suspension and settling, their large size suggests the pyrite formed in sedimentary pore fluids and comparison to modern examples suggests the sediments underlay oxic or suboxic waters (Wilkin et al., 1996). Other macro- and microscopic textures within drill-core of the Newland Formation such as

differential compaction, pyritic debris flow clasts, and detrital pyrite tube structures emphasize the early timing of pyrite formation (Fig. S5.19) (Graham et al., 2012; Present et al., in review). Pyrite and these early diagenetic textures become more prevalent in the slightly deeper waters of the Newland Formation compared to the shallow Appekunny Formation suggesting an increased flux of organic matter and potentially more reducing water column conditions aiding in preservation (e.g. Lyons et al., 2000).

Directly overlying the lower Belt strata, the Grinnell Formation and the Spokane Formation are large deposits of shallow-water hematitic siltstone and shale, and Appekunny Member 1 also contains red strata. This oxidized iron highlights the oxic nature of shallow water environments in the Belt Basin. Detrital magnetite also served as an important flux of highly reactive iron to the basin; its preservation suggests water column and pore-fluid chemistry was not rich enough in either H_2S to scavenge all of the highly reactive iron to form pyrite or ferrous iron to recrystallize the detrital magnetite to chemically precipitate authigenic magnetite (Canfield and Berner, 1987; Lyons and Severmann, 2006; Skomurski et al., 2010). Early diagenetic pyrite framboids and Fe-dolomite diagenetic cements in the lower Belt samples highlight the presence of anoxic and sulfidic pore fluid conditions, potentially extending into deep portions of the water column.

5.7 Concluding Remarks

Major first-order questions exist about the paleoredox conditions during the Proterozoic. In the present study, we use a new approach utilizing iron systematics and iron's redox sensitivity to understand paleoenvironmental conditions. Our detailed microscale textural and bulk magnetic analyses on the case-example of the mid-Proterozoic Belt Supergroup found several overprinting alterations of iron-bearing minerals. In higher-grade strata, metamorphic transformations formed pyrrhotite, siderite, and iron-silicates in the sub-biotite

zone and even in the best preserved rocks, diagenetic transformations occurred to form base-metal sulfides and nano-phase pyrrhotite. Both types of reactions probably occurred in a fluid-rich open system. Some primary minerals were preserved in the form of shallow hematite-rich red beds, ubiquitous fine-grained detrital magnetite, Fe-dolomite cements, and early diagenetic framboidal pyrite. Microscale textural observations were critical for untangling these signals to form a complete understanding of the Belt Basin. Our study concludes that deposition of the lower Belt strata occurred in oxic waters, potentially with suboxic to euxinic deep waters in permanent or episodic stratification, consistent with the results from some geochemical studies (Gellatly and Lyons, 2005; Huebschman, 1973; Luepke and Lyons, 2001; Lyons et al., 2000; Stüeken, 2013). Detrital fluxes of magnetite provided an input of highly reactive iron to the both the shallow and deep waters for the early diagenetic precipitation of pyrite in anoxic and sulfidic pore waters. Overall, this suggests a mid-Proterozoic basin chemistry inhabitable by eukaryotes that is very similar to water bodies today, in contrast to recent geochemical studies using the iron-speciation proxy which suggest predominantly ferruginous water column conditions.

Are ferruginous conditions compatible with our knowledge of microbial metabolic diversity and eukaryotic evolution by mid-Proterozoic time? Although ferrous iron will dominate ocean redox in the absence of life (Walker and Brimblecombe, 1985), upon the rise of atmospheric oxygen ~2.3 Ga, riverine input of detrital iron oxides and sulfate will substantially increase as seen in the Belt Supergroup (this study; Gellatly and Lyons, 2005; Present et al., in review). Although dissimilatory iron reduction could reduce iron oxides to maintain anoxic conditions, when sulfate is present in addition to iron (oxyhydr)oxides, fermentation and sulfate reduction metabolisms are preferred (Hansel et al., 2015; Lentini et al., 2012). All large anoxic basins in the modern are also sulfidic, e.g. the Black Sea and Cariaco Basin, due to sulfate reduction outpacing iron delivery (Berner, 1984; Lyons and Severmann, 2006), whereas the best studied modern

ferruginous basins are lakes with incredibly low sulfate concentrations comparable to Archean values even in overlying oxic waters (Crowe et al., 2014; Halevy, 2013; Koeksoy et al., 2015). Although minimal sulfate delivery to the deep ocean has been suggested for mid-Proterozoic time (Poulton and Canfield, 2011), the presence of detrital iron minerals and water-column sulfate in deep waters such as within the Belt Basin raises questions about whether ferruginous conditions could have persisted in the ocean much beyond the Great Oxidation Event.

5.8 Acknowledgements

We thank Don Winston, Jerry Zieg, Mike Jackson, Courtney Roach, John Grotzinger, Tim Lyons, Austin Chadwick, and members of the 2013 Agouron Field Course, especially Ted Present and Kirsten Siebach, for assistance during sample collection and analysis. Samples from Glacier National Park were collected under NPS Collection Permits # GLAC-2012-SCI-0195 and GLAC-2014-SCI-0008. Support for this work was provided by the Agouron Institute, Tobacco Root Geological Society Scholarship, Belt Association Student Research Grant, Geological Society of America Student Research Grant, NASA Exobiology (W.W.F.), the David and Lucile Packard Foundation (W.W.F.), NSF Graduate Research Fellowship program (S.P.S.), NASA Earth and Space Fellowship (S.P.S.), and a PEO Scholar Award (S.P.S.). Portions of this research were carried out at the Stanford Synchrotron Radiation Lightsource, a Directorate of SLAC National Accelerator Laboratory and an Office of Science User Facility operated for the U.S. Department of Energy Office of Science by Stanford University. Part of this work was performed as a US Visiting Student Fellow at the Institute for Rock Magnetism at the University of Minnesota, a US National Multi-user Facility supported through the Instrumentation and Facilities program of the National Science Foundation, Earth Sciences Division, and by funding from the University of Minnesota.

5.9 Figures

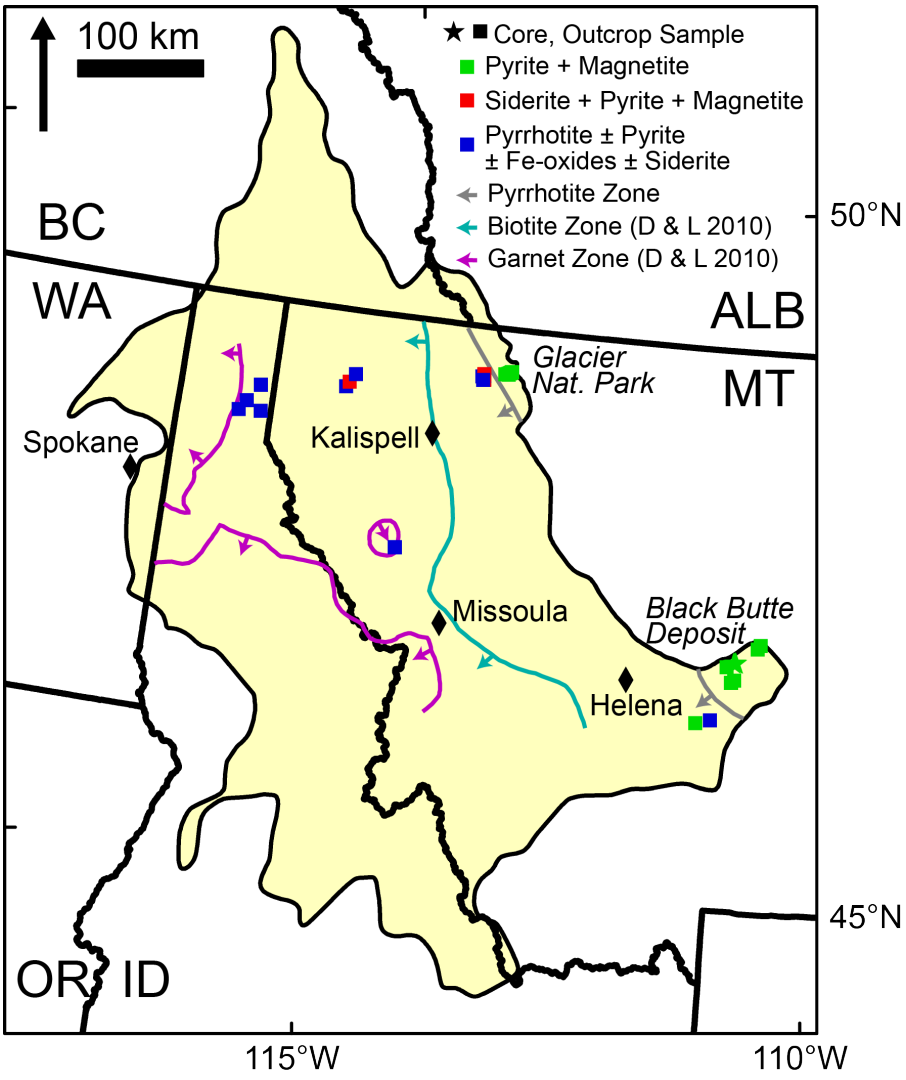

Figure 5.1: Map of the extent of the Belt Supergroup with samples from the lower Belt and Burke Formation color-coded by iron mineralogy with overlain metamorphic zone contours (this study; Duke and Lewis, 2010).

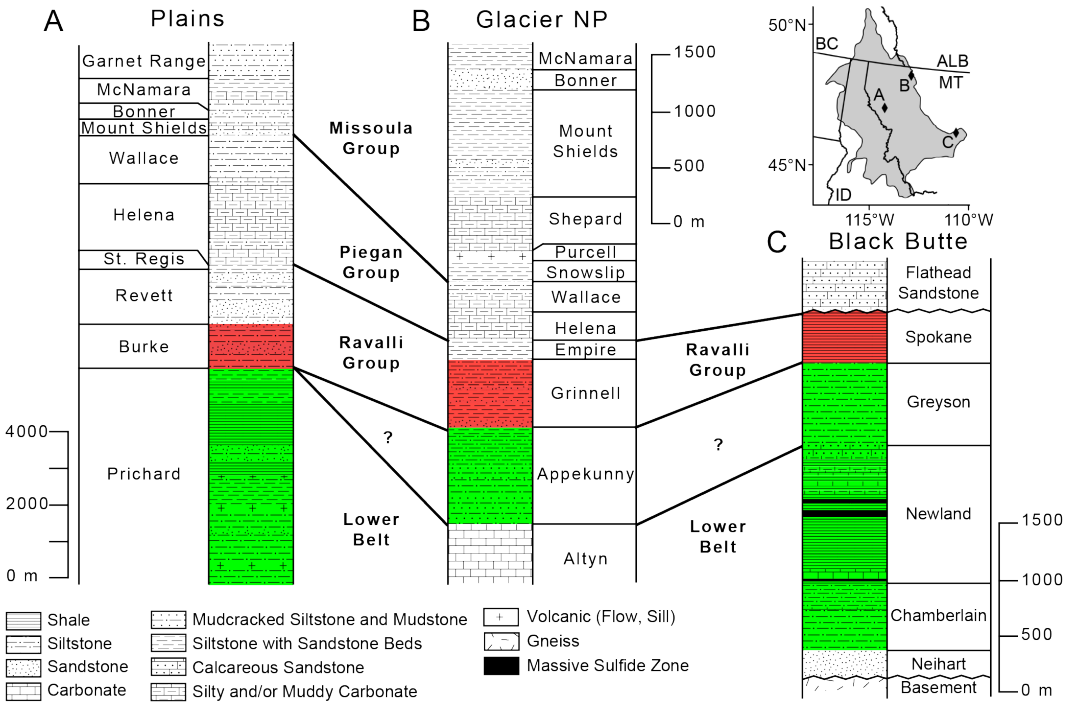

Figure 5.2: Stratigraphic nomenclature, relationships, and thickness across the Belt Basin. The lower Belt formations that are the focus of this study are shaded in green, and a few samples come from the overlying Ravalli Group formations shaded in red; these do not represent true rock color (see Fig. S5.1, S5.19). A) Stratigraphy at Plains representing nomenclature for western Montana and Idaho, B) Stratigraphy on the east side of Glacier National Park, C) Stratigraphy near the Black Butte Deposit, White Sulphur Springs representing nomenclature for the entire Helena Embayment. Note A is a different scale than B and C. Stratigraphic data from (Cressman, 1989; Harrison, 1972; Slotznick et al., 2016; Winston, 2007; Winston and Link, 1993; Zieg et al., 2013).

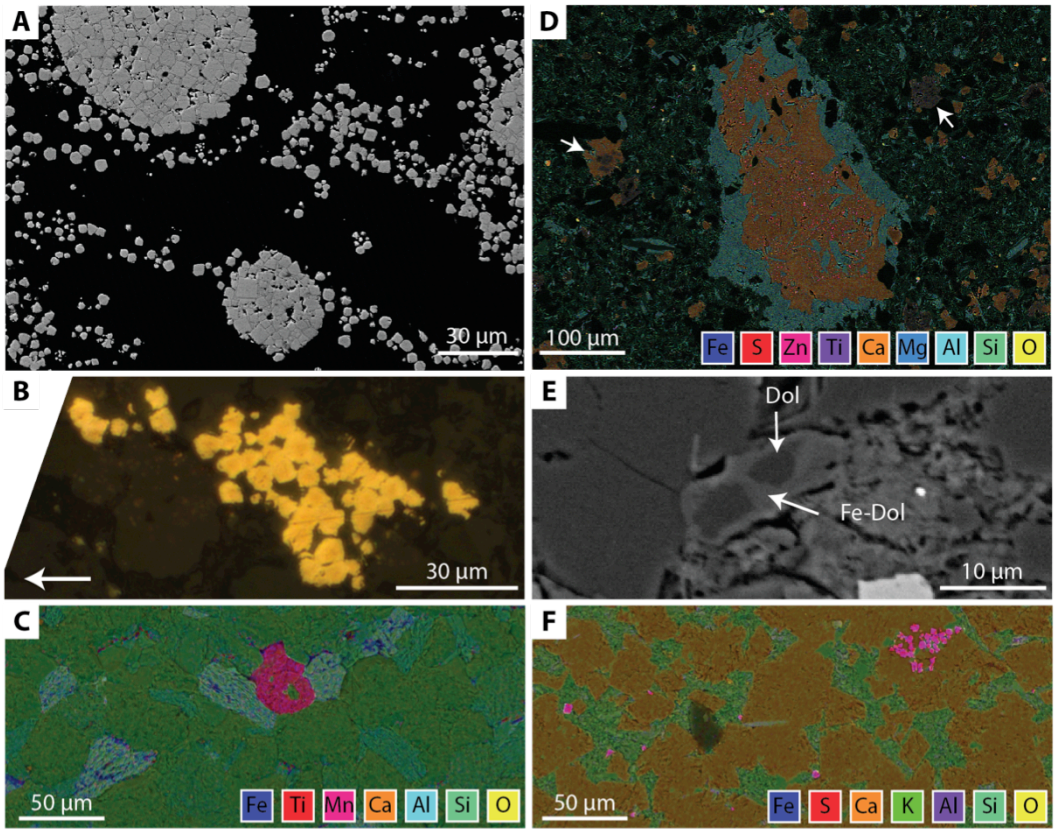

Figure 5.3: Textural examples from lower Belt samples using backscatter electron imaging, reflected light microscopy, or energy dispersive X-ray spectroscopy (EDS) overlain on backscatter images, each with own scale bar (and chemical color-code key) and all field-oriented unless otherwise stated. A) Recrystallized framboidal iron sulfides in Newland Formation, sulfide-zone Black Butte Deposit drill core sample (T095-389), B) Pyrite disaggregated framboids from Appekunny Formation, Member 3, east side of Glacier National Park (GP14-35) with arrow pointing in field up-direction, C) FeTiMnO grain and surrounding coarse-grained matrix from Prichard Formation, Transition Member, Libby (BS13-37), D) Small pyrite grains within calcite nodule rimmed by chlorite with Fe-dolomite or zoned calcite and Fe-dolomite grains pointed out with arrows in Appekunny Formation, Member 5, west side of Glacier National Park (GP14-27), E) Dolomite (Dol) rimmed by Fe-bearing dolomite (Fe-Dol) in Appekunny Formation, Member 3, east side of Glacier National Park (GP14-35), F) Fe-bearing dolomite cements in Newland Formation, far from sulfide zones in the Black Butte Deposit drill core (T112-334).

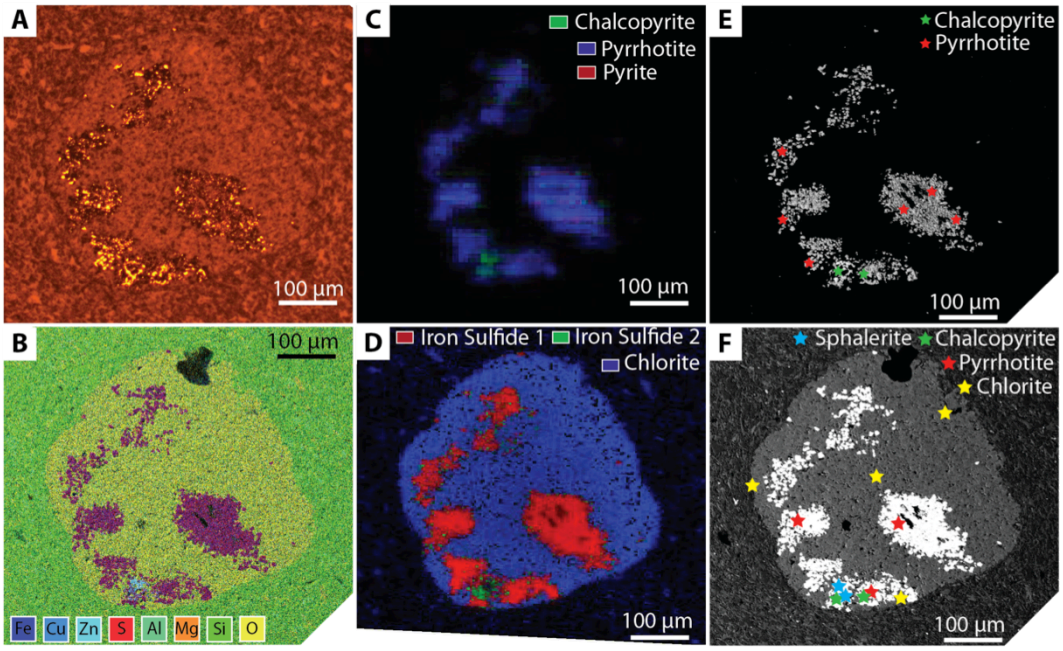

Figure 5.4: Detailed textural analysis of sample GP12-8, Appekunny Formation Member 4 or Prichard Formation, west side of Glacier National Park revealing a pyrrhotite nodule recrystallized with chalcopyrite and sphalerite inclusions and secondary chlorite replacing the original nodule. A) Reflected light microscopy, B) Energy dispersive X-ray spectroscopy (EDS), C) Synchrotron-based X-ray absorption near-edge spectroscopy (XANES) at sulfur energies, D) XANES at iron energies, E) Electron backscatter diffraction (EBSD) point mineral identifications on backscatter electron image, F) Electron probe micro-analyzer (EPMA) point mineral identifications (see Table S5.3 for details) on backscatter electron image. For XANES endmember fitted spectra, EBSD diffraction patterns, and ultrahigh resolution scanning SQuID microscope (UHRSSM) imagery see Figure S5.13.

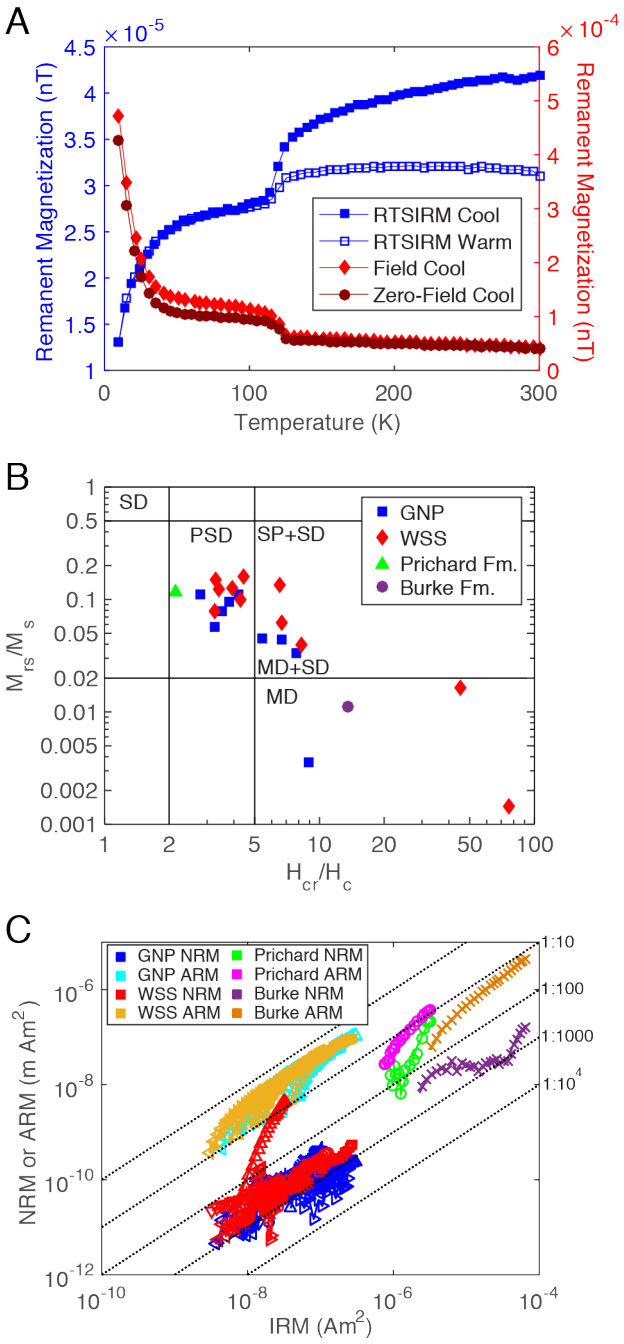

Figure 5.5: Rock magnetic measurements on samples where magnetite is the predominant ferromagnetic mineral. A) Example MPMS measurement of room temperature saturation magnetization (RTSIRM) cooling and warming, cooling in a field, and cooling in zero field on a sample from the Appekunny Formation, Member 2, Glacier National Park (GP12-1) identifying magnetite by the Verwey transition at 120 K and suggesting nanophase pyrrhotite based on the transition at

35K (Aubourg and Pozzi, 2010). More examples in Figure S5.3. B) Day Plot showing predominantly pseudo-single-domain (PSD) grain size with some multi-domain (MD) grains and possible mixtures of single-domain (SD) and MD grains. (Day et al., 1977; Dunlop, 2002) Abbreviations: SP = superparamagnetic, M_{rs} = remanent saturation magnetization, Ms = saturation magnetization, Hc = coercivity, Hcr = coercivity of remanent magnetization, GNP = Glacier National Park, WSS = White Sulphur Springs. C) Fuller Test for nature of magnetization (on all samples from part B minus one MD WSS samples and plus one GNP sample) highlights that most of the magnetite is detrital in the GNP and WSS regions based on a NRM:IRM ratio of 1:1000. The Prichard sample from Sagle Point is chemically remagnetized and the Burke sample ratio suggests a detrital remanent magnetization. (Fuller et al., 1988; Fuller et al., 2002). Abbreviations: NRM = natural remanent magnetization, IRM = isothermal remanent magnetization, ARM = anhysteretic remanent magnetization.

5.10 Supplemental Tables

Table S5.1: Detailed Sample Data for Belt Supergroup Samples*

Sample	Drill Core	Depth	GPS Location		Location†	Formation	Stratigraphic Details	Lithology
			Lat (°N)	Long (°W)				
BS13-2	--	--	46.88778	110.68635	WSS	Chamberlain	Lower (below carbonates)	Grey shale, near carbonate concretions, lenses of sand to pebble-sized siliciclastics, and rare mud cracks
BS13-1	--	--	46.91387	110.65591	WSS	Chamberlain	Upper (carbonate-rich)	Massive black dolomitic shale, interbedded with lenses of molar tooth and carbonate clasts
T029-61.08	SC11-029	61.07-61.09	46.78189	110.91287	WSS	Newland	Lower Newland right above USZ	Early diagenetic barite laths with differential compaction of laminated black and grey dolomitic shale with intergrown subparallel iron sulfide blebs
T029-76	SC11-029	76.36-76.37	46.78189	110.91287	WSS	Newland	Lower Newland in USZ	Multiple generations of iron sulfides with early unfilled circular tube network of iron sulfides <1mm in diameter and broken tubes in larger massive sulfide zone
T095-63	SC11-095	63.42-63.50	46.77910	110.92575	WSS	Newland	Upper Newland far from USZ	Early diagenetic fine-grained iron sulfide laminae showing differential compaction in laminated black and grey dolomitic shale
T095-140.08	SC11-095	140.045-140.115	46.77910	110.92575	WSS	Newland	Upper Newland SZ	Early diagenetic wrinkly iron sulfide laminations within dolomitic shale
T095-388.26	SC11-095	388.24-388.305	46.77910	110.92575	WSS	Newland	Lower Newland SZ	Early diagenetic wrinkly iron sulfide laminations including broken tubes and recrystallized framboids showing differential compaction of laminated dolomitic shale in larger massive sulfide zone
T095-388.70	SC11-095	388.70-388.73	46.77910	110.92575	WSS	Newland	Lower Newland SZ	Dolomitic shale breccia/debris flow clasts in predominantly iron sulfide matrix including early diagenetic iron sulfide broken tubes and framboids
T095-390	SC11-095	390.165-390.20	46.77910	110.92575	WSS	Newland	Lower Newland SZ	Early diagenetic fine-grained iron sulfides and recrystallized framboid laminae in dolomitic shale with broken iron sulfide tubes in massive sulfide zone
T095-400	SC11-095	400.795-400.87	46.77910	110.92575	WSS	Newland	Lower Newland right above USZ	Debris flow clasts of early diagenetic whole (<1mm) and broken iron sulfide tubes in dolomitic shale
T095-408	SC11-095	408.89-409.00	46.77910	110.92575	WSS	Newland	Lower Newland in the USZ	Multiple generations of cross-cutting sulfides (up to 1 mm blebs) including <1mm tube structures in heavily recrystallized dolomite and shale within larger massive sulfide zone
T095-410	SC11-095	410.08 - 410.11	46.77910	110.92575	WSS	Newland	Lower Newland in the USZ	Multiple generations of sulfides including 1-4mm tube structures infilled by heavily recrystallized dolomite and shale within larger massive sulfide zone
T100-407	SC12-100	407.75-407.8	46.78085	110.90605	WSS	Newland	Lower Newland right above LSZ	Secondary dolomite alteration with large (>1cm) crystals with cross-cutting secondary sulfides in laminated dolomitic shale with fine-grained iron sulfides
T101-392	SC12-101	392.125-392.15	46.78143	110.90588	WSS	Newland	Lower Newland in LSZ	Multiple generations of cross-cutting sulfides (up to 2 mm blebs) and large dolomite crystals (>1cm) in heavily recrystallized dolomite and shale within larger massive sulfide zone

Table S5.1 (Continued)

Sample	Drill Core	Depth	GPS Location		Location†	Formation	Stratigraphic Details	Lithology
			Lat (°N)	Long (°W)				
T112-345	SC12-112	345.13-345.15	46.78098	110.89963	WSS	Newland	Lower Newland in VVF Shear Zone	Black and grey laminated shale with disseminated iron sulfides
BS13-3	--	--	46.74519	110.99410	WSS	Newland	Upper Newland, Unit 5†	Orange and white sandy siltstone with even microlaminae, near ripple cross-stratification
BS13-9	--	--	46.65250	110.90630	WSS	Greyson	Upper	Grey siltstone and claystone in microlaminae and couplets with hummocky beds, gutters, and shaly parting
BS13-6	--	--	46.63475	110.93685	WSS	Spokane		Red evenly laminated interbedded siltstone and claystone with secondary (subparallel) green and orange coloration and mud cracks
BS13-8	--	--	46.63497	110.93651	WSS	Spokane		Red evenly laminated siltstone and claystone with minor orange subparallel coloration, near green mudchips
BS13-10	--	--	46.35829	111.12573	Townsend	Newland	Lower	Black dolomitic shale with faint laminations and microlenses of carbonate, near cross stratification and oolites
BS13-13	--	--	46.32876	111.27402	Townsend	Greyson	Lower	Dark grey siltstone and light grey sandstone interbedded with hummocky beds and shaly parting
PP13-6	--	--	47.36050	114.56292	Perma	Prichard	Unit F, 1.6m from sill	Grey claystone with faint laminations and weathered iron minerals and planar bedding
PP13-11	--	--	47.3603#	114.5624#	Perma	Prichard	Unit F, 25m from sill	Grey siltstone and claystone in even microlaminae with large secondary iron sulfide aggregates (>1mm), planar bedding
PP13-13	--	--	47.35963	114.56079	Perma	Prichard	Unit F, 171m from sill	Grey siltstone with faint laminations with coarse secondary mineralization (biotite?) sometimes rimming medium-sized iron sulfides (<0.5 mm), planar bedding
BS13-39	--	--	48.54377	115.20847	Libby	Prichard	Upper Member	Light grey very fine-grained sandstone with wavy lamination, thin oxidized laminae, and large (>1mm) partly oxidized iron sulfides
BS13-37	--	--	48.48608	115.26403	Libby	Prichard	Transition Member	Dark grey siltstone with faint lamination and oxidized medium (<1mm) iron sulfides
BS13-34	--	--	48.44957	115.29385	Libby	Burke		Green siltstone and claystone in even couplets with large biotite (1mm) and euhedral magnetite crystals
BS13-16	--	--	48.19321	116.15716	Lightning Ck	Prichard	Unit F	Mottled purple and green siltstone with wavy laminations and weathered out iron minerals
BS13-23	--	--	48.37509	116.19399	Lightning Ck	Prichard	Unit C	Grey fine grained sandstone with planar bedding
BS13-31	--	--	48.25364	116.31812	Hope	Prichard	Unit C	Grey very fine-grained sandstone with medium weathering iron sulfides (<.5mm), planar bedding
BS13-29	--	--	48.18188	116.39135	Sagle Pt	Prichard	Unit F	Black siltstone with very large (>2mm) secondary iron sulfide aggregates and localized alteration

*See Table A1 in Slotznick et al. (2016) for details on the 20 samples from Glacier National Park and Table 1 in Slotznick et al. (2015) for details on 11 additional samples from Black Butte drill cores
†Abbreviations: WSS= White Sulphur Springs, Ck= Creek, Pt = Point
§Zieg et al. (2015) for stratigraphic nomenclature
#Not taken in field, from Google Earth and other PP13 GPS points

Table S5.2: Mineralogy of Samples from the Belt Supergroup

Location*	Formation	Details*	Bulk Rock Magnetic Techniques†§#						
			Mag	Hem	Goe	Pyr	NP	Sid	Alloy
GNP-East	Appekunny	Mbr 1 (R)		X	X		--		
		Mbr 1 (G)	X		X		X		
		Mbr 2	X		X		X		
		Mbr 3	X		X		X		
		Mbr 4	X	X	X		X		
		Mbr 5	X				X		
	Grinnell			X	X		--		
GNP-West	Prichard	or Mbr 4	X			X			
	Appekunny	Mbr 4	X	X	X	X			
		Mbr 5	X		X			X	
White Sulphur Springs	Chamberlain		X				X		
	Newland	Outcrop	X	X	X		--		
		Diss. Core	X		X		X		
		SZ Core	X						X
	Greyson		X		X		X		
	Spokane		X	X			--		
Townsend	Newland		X	X	X	X		X	
	Greyson		X	X	X		--		
Perma	Prichard	Unit F, 171m	X					X	
		Unit F, 25m	X			X		--	
		Unit F, 1.6m	X	X		?	--	?	
Libby	Prichard		X		X	X		--	
		Transition Mbr	X	X	X		X	X	
	Burke		X			?	--	?	
Lightning Creek	Prichard	Unit C	X		X	X		X	
		Unit F	X	X		X		--	
Hope	Prichard	Unit C	X			X		--	
Sagle Pt	Prichard	Unit F	X		X	X		X	

*Abbreviations: GNP = Glacier National Park, Pt = Point, Mbr = Member, (R) = Red in color, (G) = Green in color, Diss. = Disseminated Iron Sulfides, SZ = Massive Sulfide Zone (not necessarily of economic interest)

†Abbreviations for Minerals: Mag = Magnetite, Hem = Hematite, Goe = Goethite, Pyr = Pyrrhotite, NP = nanophase pyrrhotite, Sid = siderite

§ X indicates presence of mineral, -- indicates sample was not analyzed on Magnetic Property Measurement System (MPMS) to determine if siderite or nanophase pyrrhotite were present, ? indicates within moderate Rotational Remanent Magnetization (RRM) but no additional analyses to distinguish between pyrrhotite and siderite

#Bulk Magnetic techniques for mineral identification included Coercivity spectra (Figure S5.2), RRM (Figure S5.2), MPMS (Figure S5.3), and Hysteresis loops (Figure S5.4)

Table S5.2 (Continued)

Location*	Formation	Details*	Textural Techniques†§#											
			Py	Pyr	CuPy	Gal	Sph	NiFeS	CoAsS	CuS	AgS	FerS	Bar	Su-S
GNP-East	Appekunny	Mbr 1 (R)											X	
		Mbr 1 (G)	X		X		X						X	X
		Mbr 2	X										X	
		Mbr 3	X										X	X
		Mbr 4	X				X						X	X
		Mbr 5	X		X	X	X							
	Grinnell													X
GNP-West	Prichard	or Mbr 4	X	X	X		X	X						X
	Appekunny	Mbr 4	X	X	X	X	X		X	X			X	X
		Mbr 5	X		X		X							
White Sulphur Springs	Chamberlain		X		X	X							X	
	Newland	Outcrop	X		X							X		X
		Diss. Core	X		X					X	X			X
		SZ Core	X		X	X	X					X	X	X
	Greyson		X				X							X
	Spokane													X
Townsend	Newland		X				X							X
	Greyson		X				X							X
Perma	Prichard	Unit F, 171m	X											X
		Unit F, 25m	X	X	X				X					X
		Unit F, 1.6m	X						X					X
Libby	Prichard		X		X	X	X						X	X
		Transition Mbr	X		X		X			X				X
	Burke		?	?			X							X
Lightning Creek	Prichard	Unit C		?	?		X							X
		Unit F												
Hope	Prichard	Unit C	X		X					X				X
Sagle Pt	Prichard	Unit F	X			X								X

*Abbreviations: GNP = Glacier National Park, Pt = Point, Mbr = Member, (R) = Red in color, (G) = Green in color, Diss. = Disseminated Iron Sulfides, SZ = Massive Sulfide Zone (not necessarily of economic interest)

†Abbreviations for Minerals: Py = Pyrite, Pyr = Pyrrhotite, CuPy = Chalcopyrite, Gal = Galena, Sph = Sphalerite, NiFeS = Nickel Iron Sulfide, CoAsS = Cobaly Arsenic Sulfide, CuS = Copper Sulfide, AgS = Silver Sulfide, FerS = Ferric Disulfide, Bar = Barite, Su-S = Sulfate and/or Elemental Sulfur

§ X indicates presence of mineral. Note that blank does not mean mineral is not present. ? indicates uncertainty in identification, either due to lack of structural information or lack of chemical information to provide confirmation.

#Textural techniques include X-ray absorption near-edge spectroscopy (XANES, Figure S5.5), X-ray Energy Dispersive Spectroscopy (EDS), Electron Back Scatter Diffraction (EBSD), and the Electron Probe Micro-Analyzer (EPMA, Table S3)

Table S5.2 (Continued)

Location*	Formation	Details*	Textural Techniques†§#							
			FeCrO	FeO	Fe(Mn)TiO	TiO	Fe-Dol	Chl	Ill-Bio	FeCaAlSiO
GNP-East	Appekunny	Mbr 1 (R)		X	X			X		
		Mbr 1 (G)		X		X		X	X	
		Mbr 2		X		X			X	
		Mbr 3				X	X	X	X	
		Mbr 4		X		X		X	X	
		Mbr 5				X				
	Grinnell			X	X	X				
GNP-West	Prichard	or Mbr 4		X		X		X	X	
	Appekunny	Mbr 4		X		X		X		
		Mbr 5				X	X	X	X	
White Sulphur Springs	Chamberlain		X			X		X		
	Newland	Outcrop								
		Diss. Core				X	X	X	X	
		SZ Core				X	X	X	X	
	Greyson									
	Spokane									
Townsend	Newland			X		X	X	X	X	
	Greyson									
Perma	Prichard	Unit F, 171m								
		Unit F, 25m			X	X				
		Unit F, 1.6m			X			X	X	
Libby	Prichard			X	X			X	X	X
		Transition Mbr			X			X	X	
	Burke			X		X		X	X	X
Lightning Creek	Prichard	Unit C		X	X			X	X	X
		Unit F								
Hope	Prichard	Unit C			X	X		X	X	
Sagle Pt	Prichard	Unit F				X		X		

*Abbreviations: GNP = Glacier National Park, Pt = Point, Mbr = Member, (R) = Red in color, (G) = Green in color, Diss. = Disseminated Iron Sulfides, SZ = Massive Sulfide Zone (not necessarily of economic interest)

†Abbreviations for Minerals: FeCrO = Iron Chromium Oxide, FeO = Iron Oxide, Fe(Mn)TiO = Iron Titanium Oxide with a few wt% of Manganese present in all Prichard examples, Fe-Dol = Iron-rich Dolomite, Chl = Chlorite, Ill-Bio = Illite or Biotite, FeCaAlSiO = Iron Calcium Aluminosilicate

§ X indicates presence of mineral. Note that blank does not mean mineral is not present.

#Textural techniques include X-ray absorption near-edge spectroscopy (XANES, Figure S5.5), X-ray Energy Dispersive Spectroscopy (EDS), Electron Back Scatter Diffraction (EBSD), and the Electron Probe Micro-Analyzer (EPMA, Table S3)

Table S5.3: Composition of Minerals from Select Samples of the Lower Belt Supergroup

A. SULFIDES, OXIDES, SULFATES

Sample	GP12-1	GP12-1	GP12-1	GP12-8	GP12-8	GP12-8	
Location*	GNP-East	GNP-East	GNP-East	GNP-West	GNP-West	GNP-West	
Formation†	App, Mbr 2	App, Mbr 2	App, Mbr 2	App 4/Prich	App 4/Prich	App 4/Prich	Detection Limits (wt%)#
Mineral§	Pyrite	Goethite	Fe-Sulfate	Pyrrhotite	Chalcopyrite	Sphalerite	
Fe	1.011	1.065	1.671	0.896	0.501	0.098	0.052
Cu	--	--	--	--	0.479	0.002	0.061
Zn	--	--	--	--	0.002	0.900	0.081
As	--	--	--	--	--	--	0.052
Ti	--	--	--	--	--	--	0.012
S	2.000	--	1.091	1.000	1.000	1.000	0.013
O	--	2.000	4.000	--	--	0.292	0.098
Elemental Sum (wt%)	98.822	93.065	94.206	99.244	97.668	104.005	
Number of grains	2	2	2	4	1	2	
Number of spots	4	6	3	9	2	3	

B. CARBONATES

Sample	GP12-1	GP14-35	GP14-27	GP14-35	GP14-27	T095-53	BS13-10A10	
Location*	GNP-East	GNP-East	GNP-West	GNP-East	GNP-West	WSS	Townsend	
Formation†	App, Mbr 2	App, Mbr 3	App, Mbr 5	App, Mbr 3	App, Mbr 5	Newld, Diss	Lower Newld	Detection Limits (wt%)#
Mineral**	Calcite	Calcite	Calcite	Fe-Dolomite	Fe-Dolomite	Fe-Dolomite	Dolomite	
Ca	0.978	0.976	0.974	1.028	1.184	1.019	1.031	0.010
Mg	0.013	0.016	0.011	0.871	0.550	0.829	0.937	0.014
Fe	0.009	0.008	0.015	0.101	0.265	0.152	0.033	0.033
Oxide Sum (wt%)	98.406	102.191	100.000	95.552	100.000	87.341	96.047	
Number of grains	2	2	3	2	4	5	6	
Number of spots	4	4	7	5	10	7	8	

Table S5.3 (Continued)

C. SILICATES

Sample	GP12-1	GP12-8	GP12-8	GP14-27	
Location*	GNP-East	GNP-West	GNP-West	GNP-West	
Formation†	App, Mbr 2	App 4/Prich	App 4/Prich	App, Mbr 5	Detection Limits (wt%)#
Mineral††	Illite	Illite	Chlorite	Chlorite	
Fe	0.256	0.176	1.824	2.245	0.036
Mg	0.332	0.290	2.792	2.321	0.014
Ca	0.009	0.001	0.004	0.012	0.010
Al	2.114	2.343	2.396	2.528	0.019
Ti	0.017	0.047	0.006	0.003	0.026
Na	0.008	0.015	0.010	0.007	0.021
K	0.911	0.891	0.012	0.004	0.010
Si	3.368	3.236	2.882	2.809	0.018
Oxide Sum (wt%)	95.296	95.036	85.270	85.158	
Number of grains	5	2	2	3	
Number of spots	10	3	6	10	

*Abbrevations: GNP-East = east side of Glacier National Park, GNP-West = west side of Glacier National Park, WSS = White Sulphur Springs

†Abbreviations: App = Appekunny Formation, Mbr = Member also just designated by number, Prich = Prichard Formation, Newld = Newland Formation, Diss =Disseminated sulfide drill core

§Formula for Sulfides, Oxides, and Sulfates normalized to either oxygen or sulfur in formula

#Detection Limits averaged for all spectra based on elemental or oxide weight%, -- should be interpreted as no signal above detection limit

** Calcite: cations per oxygen atom (less CO_2); (Fe-)Dolomite: cations per 2 oxygen atoms (less CO_2)

††Illite: cations per 11 oxygen atoms (less H_2O); Chlorite: cations per 14 oxygen atoms (less H_2O)

Table S5.4: Elemental abundances from X-ray fluorescence microprobe for Belt Supergroup samples*

Sample†	Location†	Formation†	Fe (wt%)	Ti (wt%)	Mn (wt%)	Cu (ppm)	Zn (ppm)	As (ppm)§	Pb (ppm)§	Ni (ppm)
GP14-10, Reg1	GNP-East	App, Mbr 1 (G)	4.68	0.192	--	40.9	282	38.7	255	559
GP12-1, Reg4	GNP-East	App, Mbr 2	3.54	0.213	0.000056	21.7	143	40.1	--	237
GP14-35, Reg1	GNP-East	App, Mbr 3	4.99	0.190	--	27.1	229	36.9	242	565
GP14-30, Reg1	GNP-East	App, Mbr 4	3.06	0.183	--	28.61	165	29.9	196	324
GP14-33, Reg2	GNP-East	App, Mbr 5	10.4	0.474	0.273	47.4	362	92.3	543	986
GP12-8, Reg1	GNP-West	Prich/App, Mbr 4	2.01	0.232	0.042	21.3	106	42.7	--	131
GP14-55, Reg1#	GNP-West	App, Mbr 4	10.3	0.147	0.235	161	570	752	5432	1513
GP14-28, Reg1	GNP-West	App, Mbr 5	8.74	0.339	--	48.8	343	46.1	303	1011
GP14-54, Reg1#	GNP-West	App, Mbr 5	5.44	0.150	--	33.4	360	49	353	748
Average Published Appekunny Formation Data**			2.59±0.55	0.294±0.045	0.037±0.024	12.4±11.0	58.3±18.3	2.57±1.41	8.03±4.53	22.6±8.33
GP14-8, Reg1	GNP-East	App, Mbr 1 (R)	8.74	0.474	0.224	46.4	340	96.6	569	813
GP12-2, Reg1	GNP-East	Grinnell	3.82	0.258	0.126	65.7	1310	101	593	363
BS13-6, Reg1	WSS	Spokane	3.56	0.269	0.217	59.9	249	9795	57699	390
Average Published Grinnell Formation Data††			3.26±0.925	0.316±0.030	0.068±0.113	4.52±4.29	58.8±20.6	4.90±2.53	12.3±4.22	20.4±4.86
T095_38#	WSS	Newld, Diss. Core	3.41	0.049	0.365	41.1	423	155	1006	417
T095_53#	WSS	Newld, Diss. Core	6.42	0.143	0.120	118	282	154	1114	875
T112_334#	WSS	Newld, Diss. Core	4.70	0.048	0.372	47.5	71.4	115	828	691
T112_384#	WSS	Newld, Diss. Core	4.33	0.109	0.071	40.9	232	108	697	540
T029_56	WSS	Newld, SZ Core	7.00	0.176	0.118	1153	318	924	5153	767
T095_140.36	WSS	Newld, SZ Core	18.2	0.483	0.386	101	229	1227	6921	1940
T101_389	WSS	Newld, SZ Core	8.89	0.189	0.155	3409	496	362	1646	987
Average Published Newland Formation Data§§			2.23±0.415	--	--	--	110±105	--	--	--
BS13-2, Reg1#	WSS	Chamberlain	12.3	0.231	0.247	139	300	84	560	1412
BS13-13, Reg1#	Townsend	Greyson	6.38	0.209	0.132	85.9	341	124	802	65
PP13-13, Reg2#	Perma	Prich, Unit F, 171m	4.21	0.104	0.0978	44.2	380	49.4	357	575
PP13-11, Reg1#	Perma	Prich, Unit F, 25m	9.52	0.175	0.227	149	529	132	853	1300
PP13-6, Reg1#	Perma	Prich, Unit F, 1.6m	3.95	0.086	0.088	37.3	228	65.1	471	496
BS13-37, Reg1#	Libby	Prich, Trans Mbr	6.14	0.113	0.150	142	489	67.0	484	892
BS13-31, Reg1#	Hope	Prich, Unit C	10.3	0.341	0.219	302	756	379	6481	1638
BS13-29, Reg1#	Sagle Pt	Prich, Unit F	1.78	0.051	0.032	35.0	99.8	94.2	1545	270

*For detailed explanation of methodology to produce this data see Slotznick et al. (2016). X-ray fluorescence maps used for calculations are in Figures S5.6-S5.9.

†Reg = scanned region on thin or thick section, GNP-East = East side of Glacier National Park, GNP-West = West side of Glacier National Park, WSS =White Sulphur Springs, Ck = Creek, Pt = Point, App = Appekunny Formation, Mbr = Member, Newld = Newland Formation, Prich = Prichard Formation,

§As and Pb energy windows overlap in XRF so most samples are a mixture of these two minerals, each calculation assumes the channel is solely for As or Pb. -- when Pb standard not run for calculations

Thick section (3-8.5 mm) instead of thin section (20-30 μm); since homogeneous correction is made assuming same material across entire depth this could lead to larger error in calculation

** Data from silt and claystones of González-Álvarez et al. (2006) and González-Álvarez and Kerrich (2010) averaged with 1 population standard deviation, n= 16 for Fe, Ti, Mn, As, and Ni, n = 12 for Cu and Zn

†† Data from silt and claystones of González-Álvarez et al. (2006) and González-Álvarez and Kerrich (2010) averaged with 1 population standard deviation, n= 10 for Fe, Ti, Mn, As, Pb, and Ni, n = 6 for Cu and Zn

§§ Data from SC93 drill core samples of Planavsky et al. (2011) averaged with 1 population standard deviation, n=7. Note Zn was measured as a proxy for alteration and one can see from our data that it is not an important mineral signaling secondary mineralization

Table S5.5: Hysteresis magnetic parameters for dominantly magnetite-bearing Belt Supergroup Samples with calculated magnetite content

Sample	Location*	Formation, Details*	Ms (Am/kg)	Mr (Am/kg)	Hc (mT)	Hcr (mT)	Magnetite (ppm)
GP14-10	GNP-East	Appekunny, Mbr 1	0.000225014	2.13434E-05	10.3396	39.571	2.4458
GP12-1	GNP-East	Appekunny, Mbr 2	0.000470666	5.21753E-05	12.4585	52.9032	5.1159
GP14-11	GNP-East	Appekunny, Mbr 2	0.00018216	2.01237E-05	12.8275	36.0801	1.9800
GP14-34	GNP-East	Appekunny, Mbr 3	0.000476883	2.13196E-05	7.72136	42.1604	5.1835
GP14-35	GNP-East	Appekunny, Mbr 3	0.000720169	0.000031621	5.74438	38.8214	7.8279
GP14-29	GNP-East	Appekunny, Mbr 4	0.000337311	1.17617E-06	5.03967	45.2754	3.6664
GP14-30	GNP-East	Appekunny, Mbr 4	0.000337506	2.61416E-05	11.3329	40.2592	3.6685
GP14-32	GNP-East	Appekunny, Mbr 5	0.000184434	1.04356E-05	11.741	38.6041	2.0047
GP14-33	GNP-East	Appekunny, Mbr 5	0.00038637	1.28502E-05	5.65243	44.5852	4.1997
GP14-54	GNP-West	Appekunny, Mbr 5	0.000191623	-1.17473E-07	2.57526	55.7777	2.0829
BS13-1	WSS	Chamberlain	0.000120955	1.20091E-05	8.54055	37.0†	1.3147
BS13-2	WSS	Chamberlain	0.000381684	1.51018E-05	4.83784	40.1†	4.1487
T112_334	WSS	Newland, Diss. Core	0.000145519	9.00742E-06	6.9962	47.2†	1.5817
T112_345	WSS	Newland, Diss. Core	0.000263676	3.32256E-05	11.9087	47.3916	2.8660
T112_384	WSS	Newland, Diss. Core	0.000174942	2.51843E-07	0.465604	36.0557	1.9015
T095_53	WSS	Newland, Diss. Core	0.000414195	5.12036E-05	12.2904	42.3†	4.5021
T095_63	WSS	Newland, Diss. Core	0.000263349	4.17803E-05	10.2505	46.0†	2.8625
T029_61.08	WSS	Newland, USZ Core	0.000088051	1.18154E-05	6.93643	45.8162	0.9571
T029_61.21	WSS	Newland, USZ Core	0.000108826	1.62341E-05	13.2581	44.2799	1.1829
T100_407	WSS	Newland, LSZ Core	0.000420261	6.85198E-06	1.37417	63.1387	4.5681
BS13-9	WSS	Greyson	0.00028543	2.21245E-05	11.9577	39.2776	3.1025
BS13-29	Sagle Pt	Prichard, Unit F	0.00038247	4.47785E-05	22.0431	47.4701	4.1573
BS13-34	Libby	Burke	1.14258	0.0125691	1.9211	26.3241	1.2419%§

Note: Ms is saturation magnetization, Mr is remanent saturation magnetization, Hc is coercivity, and Hcr is coercivity of remanent magnetization (using backfield method). Magnetite content is calculated following Klein et al. (2014) by dividing the Ms by Ms value for pure magnetite (92 Am/kg).

*Abbreviations: GNP = Glacier National park, WSS = White Sulphur Springs, Pt = Point, Mbr = Member, Diss. = Disseminated Iron Sulfides, USZ = Upper Sulfide Zone, LSZ =Lower Sulfide Zone

†Measured on 2G SQuID Magnetometer on neighboring slice instead of on VSM like all other measurements.

§Note: This is in weight percent as opposed to ppm like the rest of the data.

5.11 Supplemental Figures

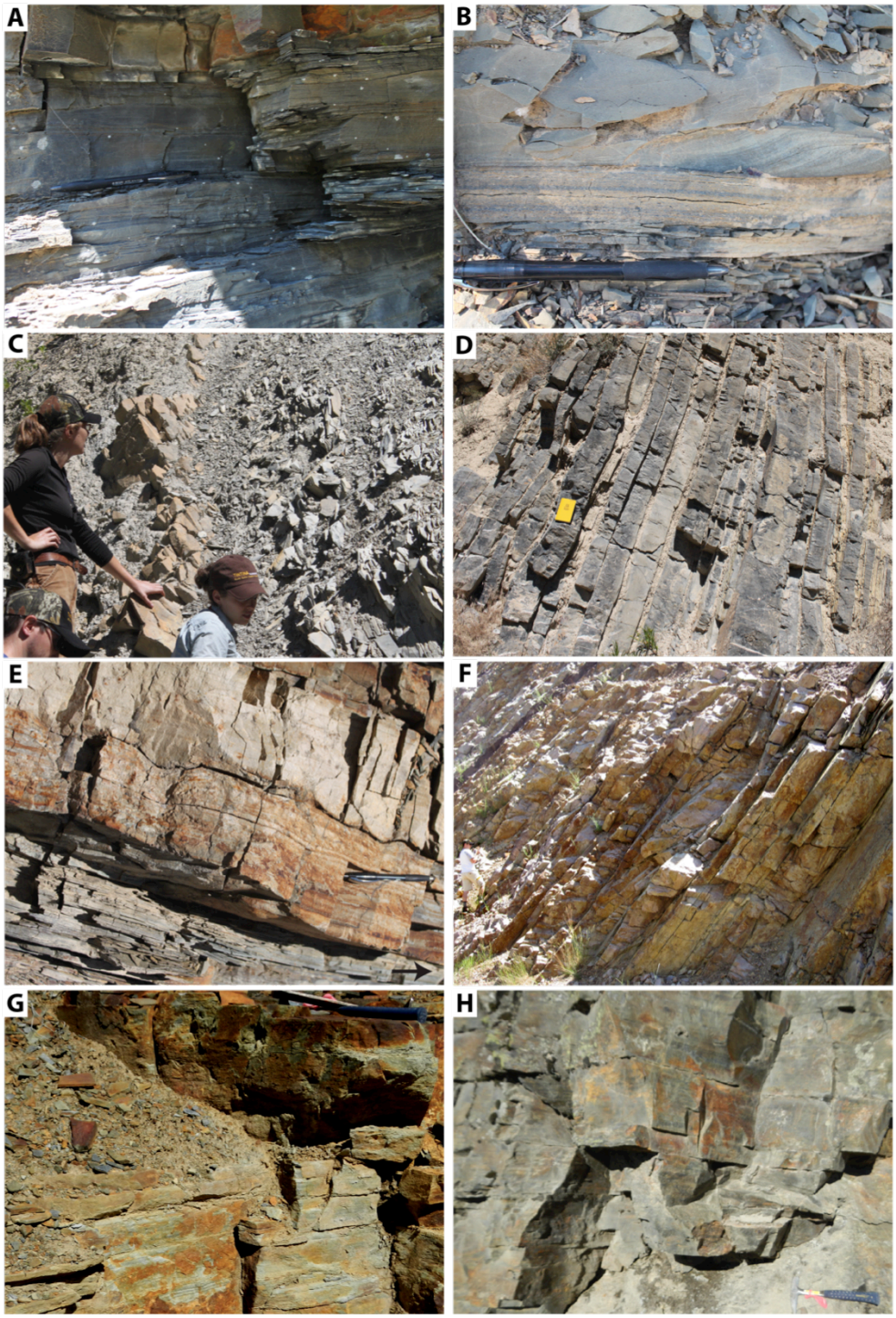

Figure S5.1: Photographs of the lower Belt Supergroup outcrops in the Helena Embayment and western Montana and Idaho. See Slotznick et al. (2016) for

images of lithologies from Glacier National Park. A) Grey, finely laminated shale and siltstone with decimeter-scale hummocky cross-stratification and early carbonate concretions causing differential compaction in the Lower Chamberlain Formation, White Sulphur Springs. Pen is 15 cm for scale. B) Finely laminated grey shale and siltstone displaying ripple-cross stratification in the Upper Newland Formation, Unit 5, White Sulphur Springs. Pen is 15 cm for scale. C) Interbedded black dolomitic shale displaying shaly parting and blocky carbonate-rich sandstone in Lower Newland Formation, Townsend. People for scale. D) Interbedded dark grey carbonate and shale beds showing meter-scale hummocky cross-stratification in the Upper Newland Formation, Unit 3, Townsend. Rite-in-the-Rain notebook is 19 cm tall for scale. E) Interbedded finely laminated dark grey siltstone-claystone and light grey sandstone showing decimeter-scale hummocky cross stratification and shaly parting in the Lower Greyson Formation, Townsend. Note the individual red iron oxides from the surface weathering of iron sulfides. Beds are steeply dipping in this location, with field up-direction noted by arrow. Pen is 15 cm for scale. F) Thick planer bedded grey siltstone and claystone with reddish-orange surface-weathering varnish of the Prichard Formation, Unit F, Perma. Person in lower left for scale. G) Even to wavy couplets of light grey very fine-grained sandstone and dark grey siltstone and claystone showing blocky planar bedding and reddish-orange surface-weathering varnish in the Prichard Formation, Upper Member, Libby. Hammer (under chisel) is 33 cm for scale. H) Even couplets of grey very fine-grained sandstone and silt-claystone in blocky planar beds of the Prichard Formation, Unit C, Hope. Hammer is 33 cm for scale.

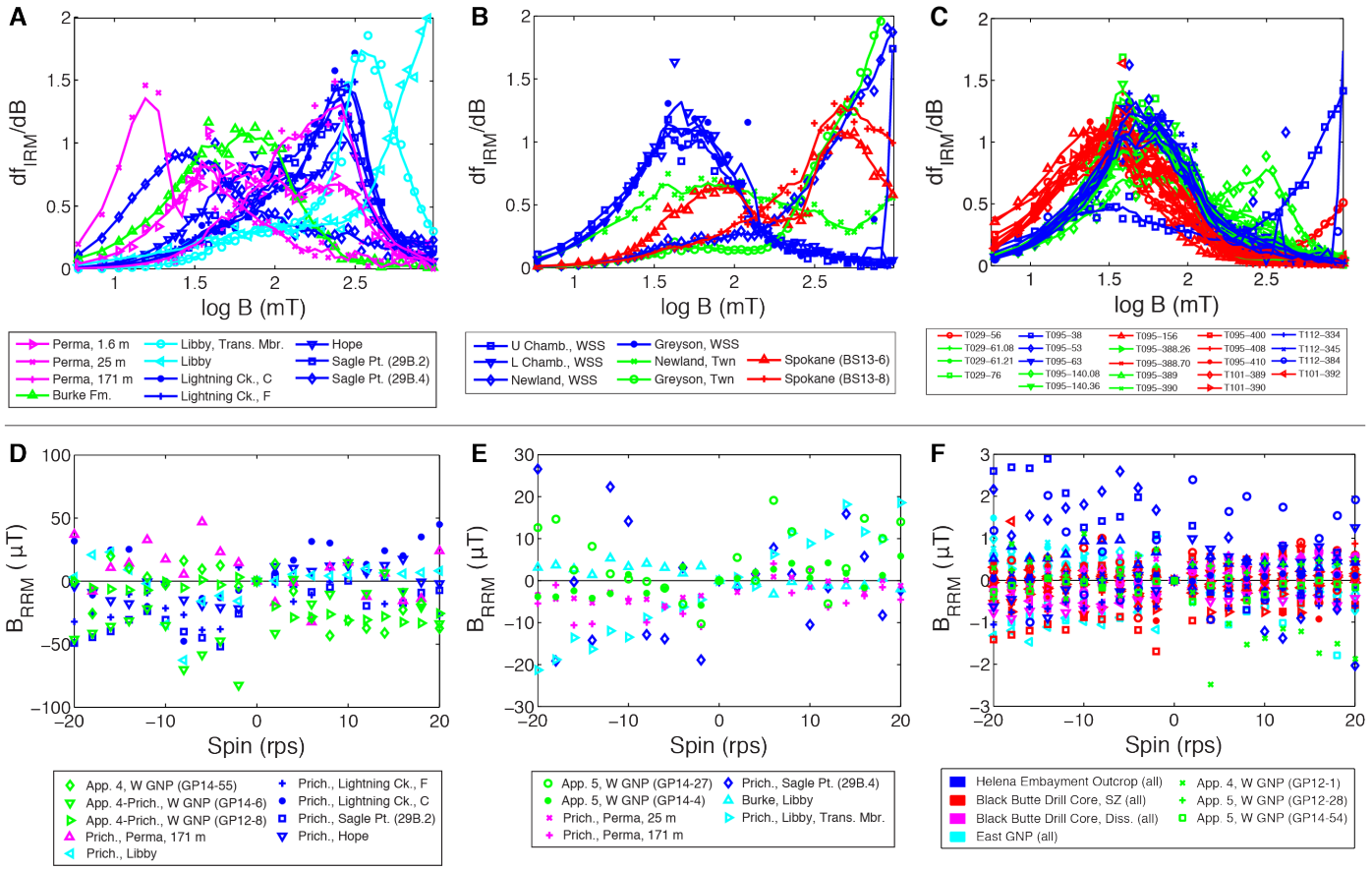

Figure S5.2: A-C) Coercivity of remanence spectra created from the derivative of the isothermal remanent magnetization (IRM) to the applied field (B) to determine ferromagnetic mineralogy (Heslop et al., 2002; Robertson and France, 1994). The samples from the

Prichard Formation (part A), Burke Formation (part A), and Helena Embayment Outcrop Samples (part B) are color-coded by location. The Black Butte drill core samples (part C) are color-coded by disseminated pyrite core in blue, sulfide zone core in red or green if the coercivity is changed by the unknown low-coercivity (alloy?) phase. All sulfide zone drill-core samples were shown to contain the unknown low-coercivity phase in hysteresis diagrams. For data from Glacier National Park, see Slotznick et al. (2016) and eight of the spectra in part C were previously published in Slotznick et al. (2015). D-F) Presence of rotational remanent magnetization (RRM) here shown as deviation from zero by B_{RRM} to identify magnetic iron sulfides and siderite (Snowball, 1997; Thomson, 1990). D) Samples with a strong RRM ($B_{RRM} > \pm 20$ μT at 5 rps) contain pyrrhotite (Potter and Stephenson, 1986; Suzuki et al., 2006). E) Samples with a moderate RRM may contain pyrrhotite or siderite. F) Samples with no RRM ($B_{RRM} < \pm 3$ μT at 5 rps) do not contain pyrrhotite. Samples are color-coded by region, although part F uses a different color-code. Legend abbreviations used: Fm. —Formation, Trans. Mbr. —Transition Member, Ck. —Creek, Pt.—Point, C—Prichard Formation, Unit C, F—Prichard Formation Unit F, Chamb.—Chamberlain, Twn—Townsend, U—Upper, L—lower, WSS—White Sulfur Springs, App. —Appekunny Formation (and following number is Member), Prich.—Prichard Formation, W GNP—west side of Glacier National Park. If two samples have the same location and formation description, sample number is also shown.

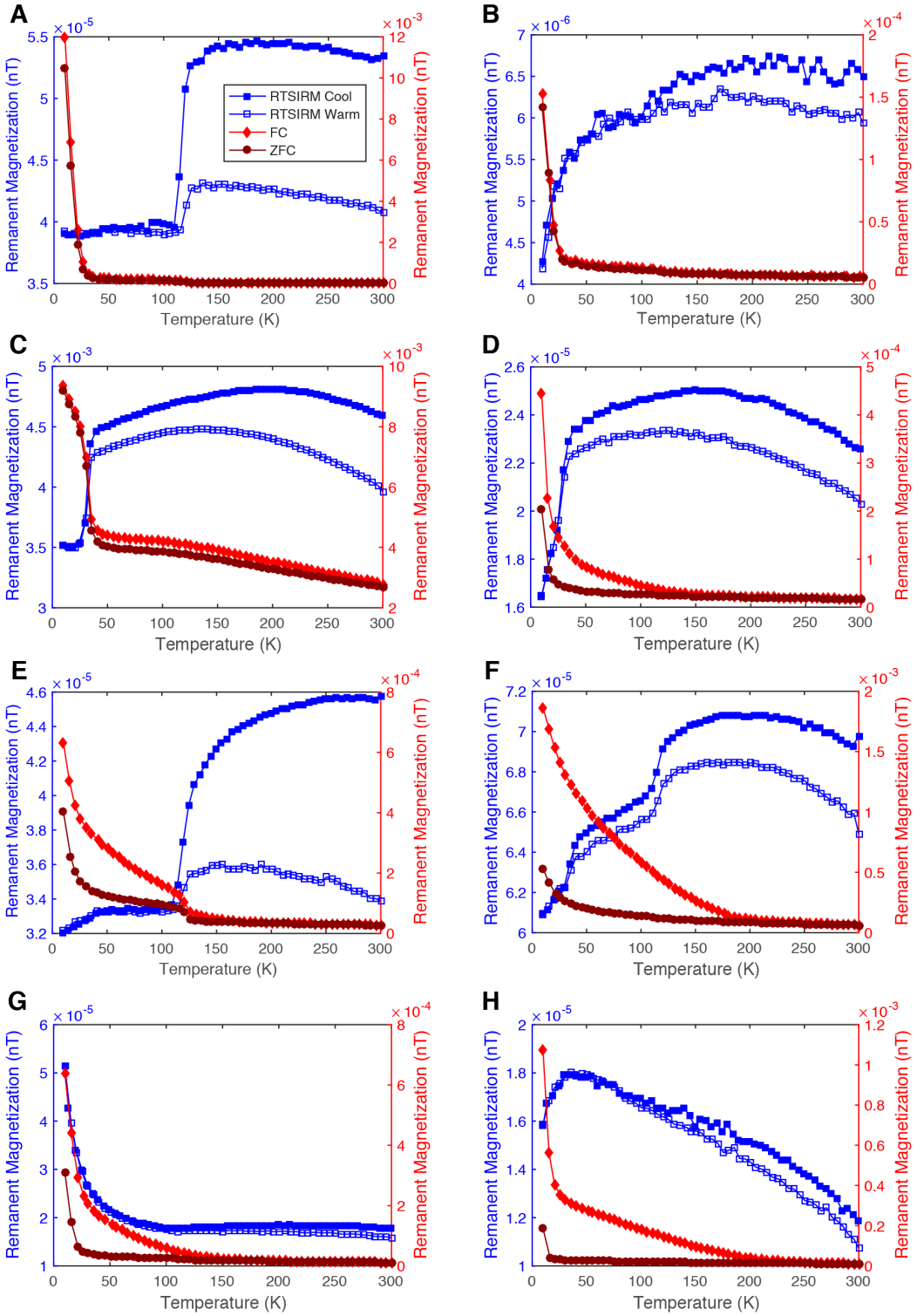

Figure S5.3: Additional example MPMS measurements of room temperature saturation magnetization (RTSIRM) cooling and warming, cooling in a field (FC),

and cooling in zero field (ZFC) for 8 out of the 21 lower Belt samples measured, spanning a variety of mineralogies and mineral mixtures. Key for all plots is in part A, and RTSIRM are scaled to left Y-axis while FC and ZFC are scaled to the right. A) Magnetite from the Verwey transition at 120K (Verwey, 1939) as well as a low-temperature ordering/blocking phase are present in T095-156, Newland Fm. (Fm.), Massive Sulfide Zone drill core, White Sulphur Springs. B) Nano-phase pyrrhotite dominates the magnetic signal with a sudden reversible transition in RTSIRM at 35K and nearly indistinguishable FC and ZFC below this transition (Aubourg and Pozzi, 2010) in sample T112-334, Newland Fm., disseminated sulfide drill core, White Sulphur Springs. A very small Verwey transition i.e. a small amount of magnetite is present as well. C) Pyrrhotite showing classic Besnus transition at 32K (Besnus and Meyer, 1964; Rochette et al., 1990) is identified in GP12-8, Appekunny Fm., Member 4 or Prichard, west side of Glacier National Park. D) Pyrrhotite mixed with goethite, identified by its exponential rise starting at 150K in FC >ZFC (e.g. Liu et al., 2006), and siderite, identified by transitions at its Néel temperature of 37K with FC>ZFC (Hilscher et al., 2005; Housen et al., 1996), were found in BS13-23, Prichard Fm., Unit C, Lightning Creek. E) Magnetite is present as well as goethite and nano-phase pyrrhotite in BS13-9, Greyson Fm., White Sulphur Springs. F) A complex but identifiable mixture of magnetite, goethite, pyrrhotite and potentially siderite are present in BS13-10, Newland Fm., Townsend. G) Goethite and siderite are present with superparamagnetic minerals (maybe nano-phase magnetite with rise in RTSIRM at ~100K) and a very small amount of magnetite in GP14-27A, Appekunny Fm., Member 5, west side of Glacier National Park. H) Mixture of goethite, siderite, nanophase pyrrhotite, and very small amount of magnetite are identified in sample BS13-37, Prichard Fm., transition member, Libby.

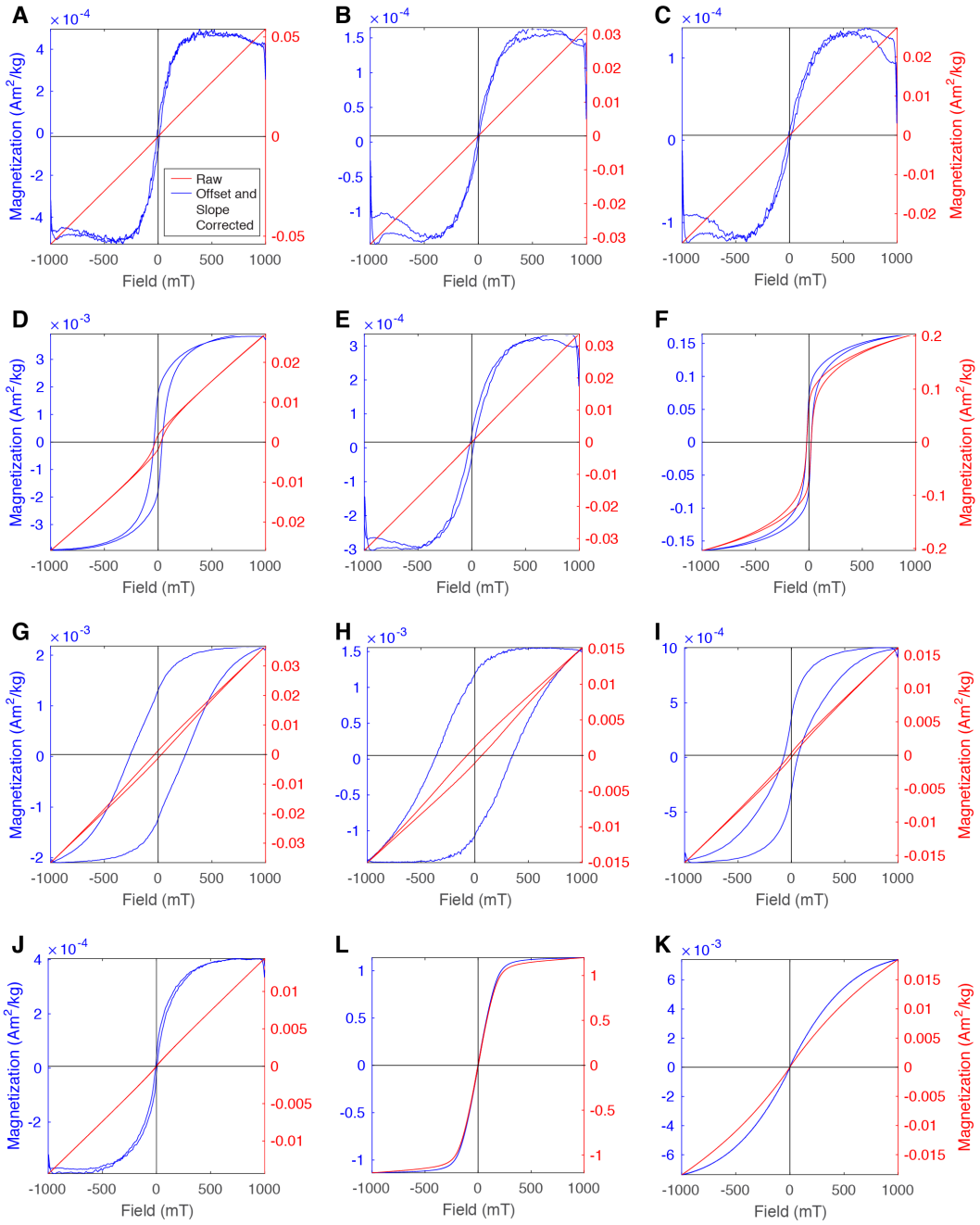

Figure S5.4: Example hysteresis loops displaying the range of magnetic mineralogies identified by shape, coercivity, and field of saturation in the 63 samples measured (e.g. Roberts et al., 2006; Tauxe et al., 1996). The raw data highlights the large proportion of paramagnetic minerals in the samples. A) Pseudo-single-domain (PSD) magnetite in GP12-1 Appekunny Formation (Fm.),

Member 2, east side of Glacier National Park. B) PSD magnetite in T112-334, Newland Fm., disseminated sulfide drill core, White Sulphur Springs. C) PSD magnetite in BS13-37, Prichard Fm., Transition Member, Libby. D) Pyrrhotite in GP12-8, Appekunny Fm., Member 4 or Prichard, west side of Glacier National Park. E) Pyrrhotite and magnetite mixture in GP14-6, Appekunny Fm., Member 4 or Prichard, west side of Glacier National Park. F) Pyrrhotite with multi-domain (MD) magnetite in PP13-11, Prichard Fm., Unit F, 25m from sill, Perma. G) Hematite in GP14-8, Appekunny Fm., Member 1 Red, east side of Glacier National Park. H) Hematite and goethite in GP12-2A, Grinnell Fm., east side of Glacier National Park. I) Hematite and magnetite mixture in BS13-6, Spokane Fm., White Sulphur Springs. J) PSD magnetite and SD magnetite mixture, BS13-10, lower Newland Fm., Townsend. K) MD magnetite in BS13-34, Burke Fm., Libby. L) Unknown magnetic mineral, perhaps an alloy, with low coercivity but high saturation field in T095-156, Newland Fm., sulfide zone drill core, White Sulphur Springs.

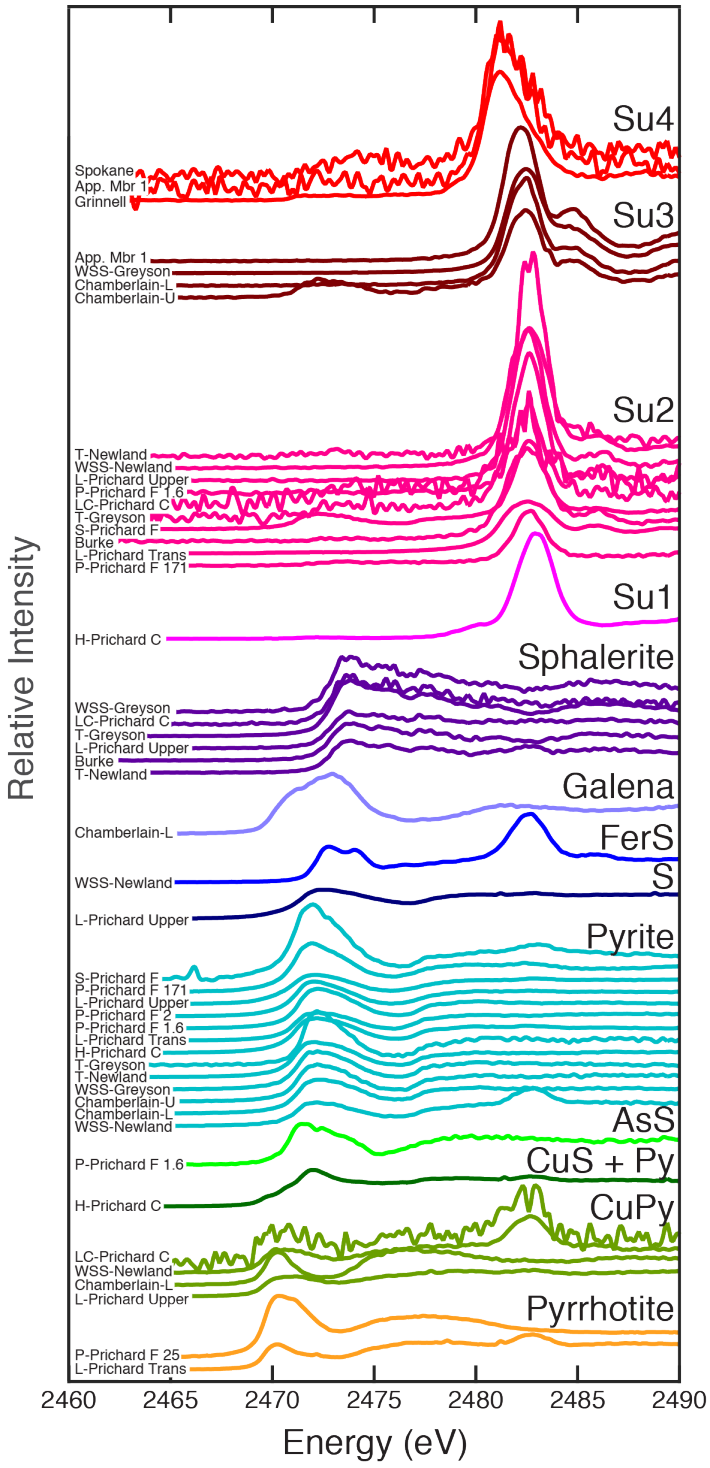

Figure S5.5: End-member X-ray absorption near-edge spectra (XANES) for samples of the Prichard Formation, Burke Formation, outcrop samples from the

Helena Embayment, and red-beds in Glacier National Park grouped based on mineralogy. Note that there are 4 different types of sulfates found in the specimens based on slightly different spectra. Mineralogy abbreviations: CuPy–chalcopyrite, CuS + Py—copper disulfide (either chalcocite or chalcopyrite) mixed with pyrite, AsS—arsenic disulfide, S—elemental sulfur, FerS—ferric disulfide, Su1—sulfate 1, Su2—sulfate 2, Su3—sulfate 3, Su4—sulfate 4. Location and sample abbreviations: App.—Appekunny Formation, Mbr—Member, WSS—White Sulphur Springs, L—Lower Chamberlain Formation, U—Upper Chamberlain Formation, T—Townsend, L—Libby, P—Perma, LC—Lightning Creek, H—Hope, C—Prichard Unit C, F—Prichard Unit F, 1.6—1.6 m from sill, 25—25 m from sill, 171—171 m from sill, S—Sagle Point, Trans—Prichard Formation Transition Member. For additional XANES endmember spectra from the rest of the Belt Basin that informed mineralogy in Table S5.2, see Slotznick et al. (2015) and Slotznick et al. (2016).

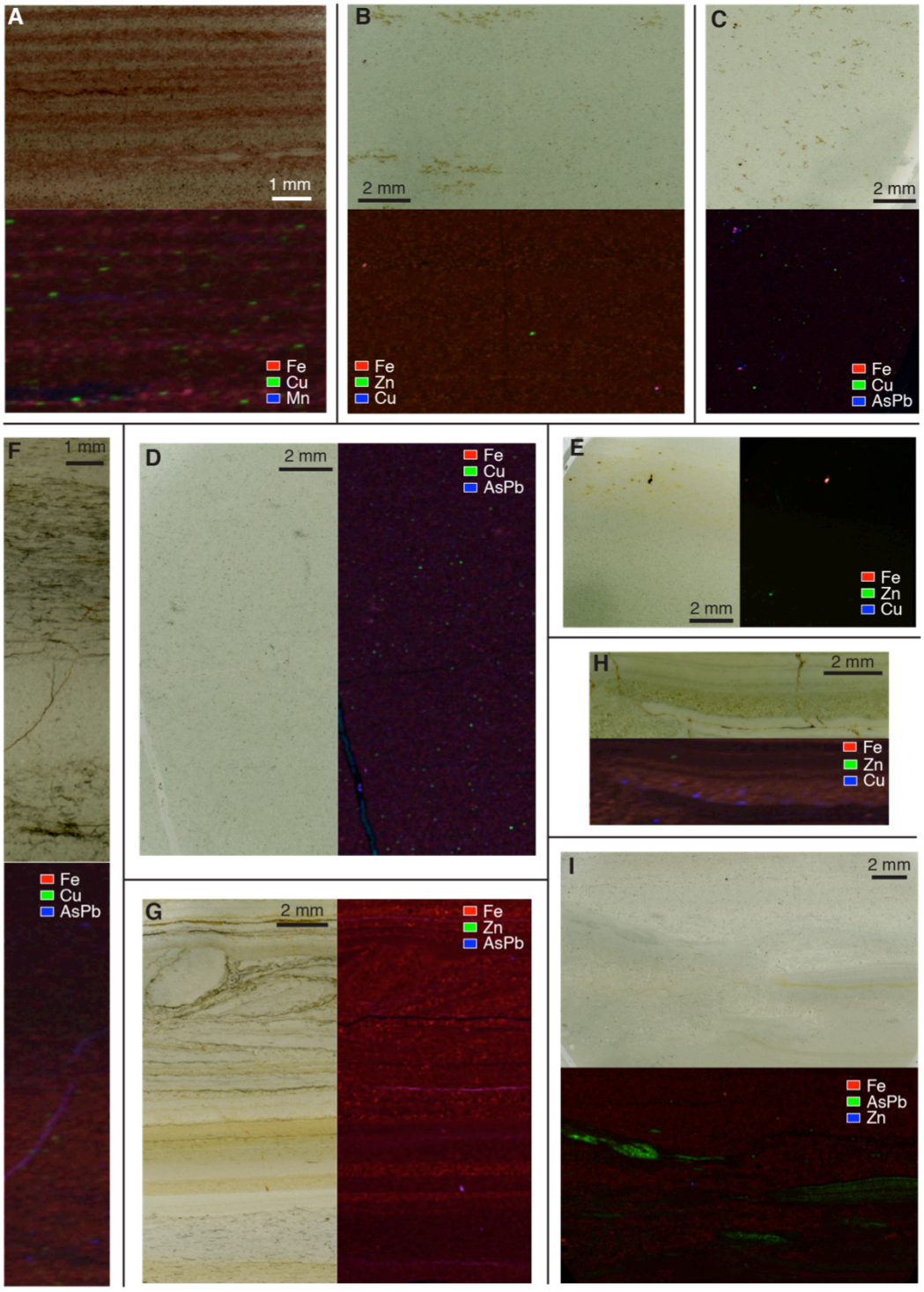

Figure S5.6: High-energy X-ray fluorescence (XRF) maps displaying elemental abundances paired with scans of the corresponding thin section region in the

Appekunny Formation on the east side of Glacier National Park. Separate scale bar and element key for each image pair (black to brightly colored at maximum). A) GP14-8, Member 1, Red. B) GP14-10, Member 1, Green. C) GP14-11, Member 2. D) GP14-35, Member 3. E) GP14-34, Member 4. F) GP14-29, Member 4. G) GP14-30, Member 4. H) GP14-33, Member 5. I) GP14-32, Member 5. A, B, D, G, H were used for elemental abundance quantification in Table S5.4. See Slotznick et al. (2016) for XRF map of GP12-1, Member 2 and sample details.

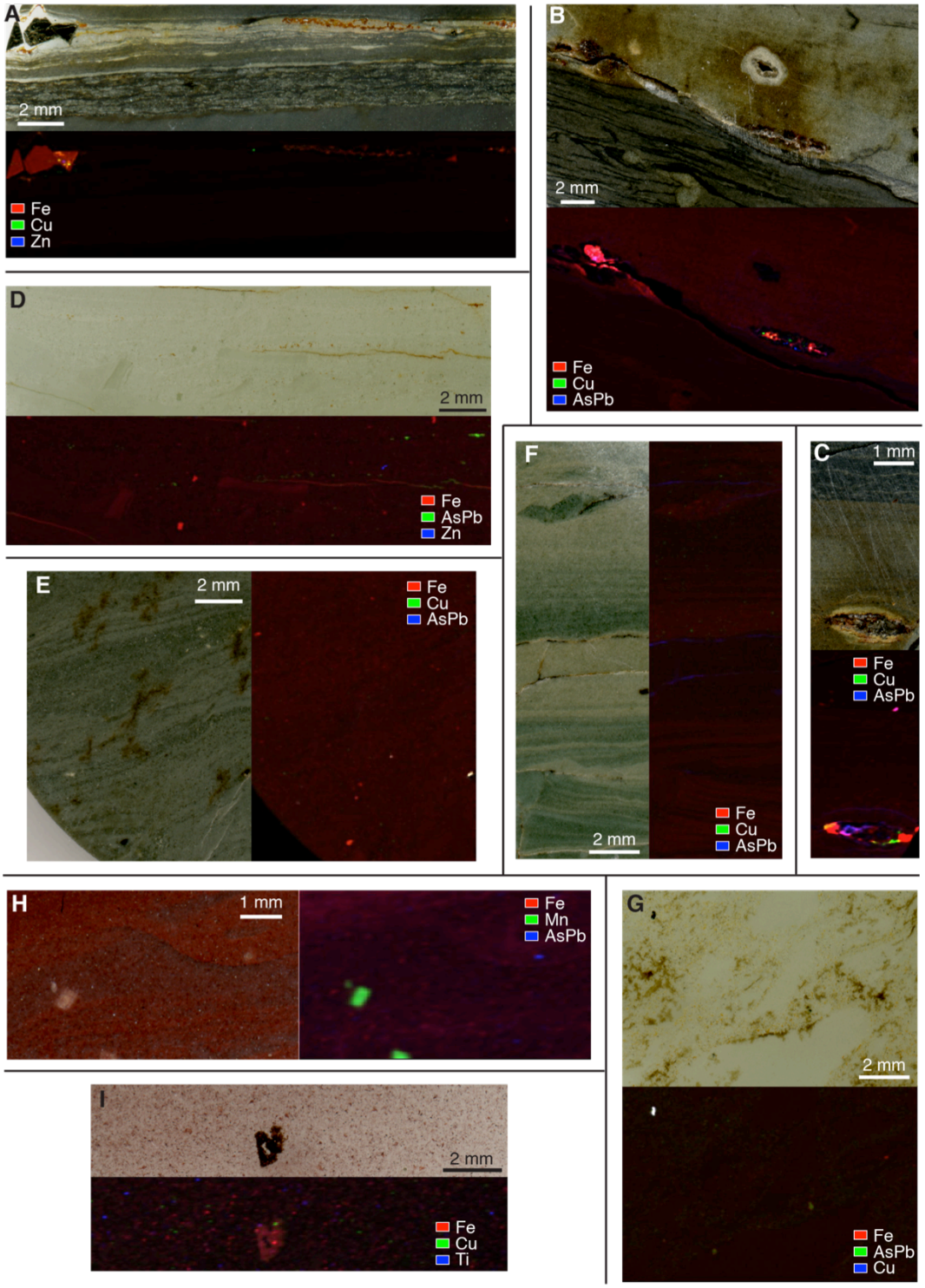

Figure S5.7: High-energy X-ray fluorescence (XRF) maps displaying elemental abundances paired with scans of the corresponding thick or thin section region in

the Appekunny Formation on the west side of Glacier National Park and the Grinnell Formation on the east side of Glacier National Park. Separate scale bar and element key for each image pair (black to brightly colored at maximum). A) GP14-6, Prichard or Member 4, West Mt. Brown. B) GP14-55, Member 4, East Mt. Brown. C) GP14-1, Member 4, East Mt. Brown. D) GP14-28, Member 5, McDonald Creek. E) GP14-4, Member 5, East Mt. Brown. F) GP14-54, Member 5, East Mt. Brown. G) GP14-27, Member 5, McDonald Creek. H) GP12-3, Grinnell Formation. I) GP12-2, Grinnell Formation. B, D, F, I were used for elemental abundance quantification in Table S5.4. See Slotznick et al. (2016) for XRF map of GP12-8, Prichard or Appekunny Member 4 and sample details.

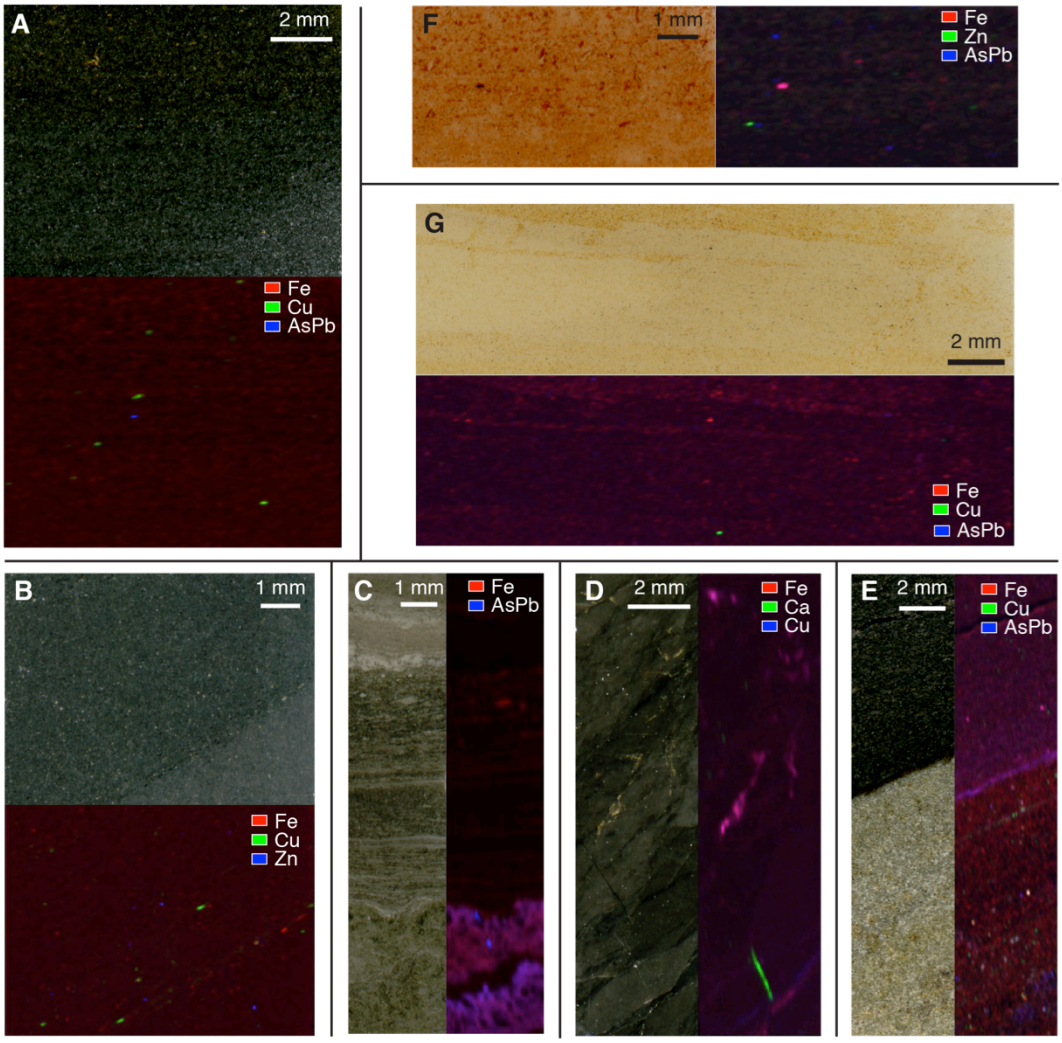

Figure S5.8: High-energy X-ray fluorescence (XRF) maps displaying elemental abundances paired with scans of the corresponding thin or thick section region in the samples from the Helena Embayment. Separate scale bar and element key for each image pair (black to brightly colored at maximum). Images for Black Butte drill core samples are brightened to highlight subtle sedimentary features. A) BS13-2, Chamberlain Formation, White Sulphur Springs. B) T095-53, Newland Formation, Disseminated Pyrite Core, White Sulphur Springs. C) T095-140.36, Newland Formation, Sulfide Zone Core, White Sulphur Springs. D) T112-384, Newland Formation, Disseminated Pyrite Core, White Sulphur Springs. E) BS13-13, Greyson Formation, Townsend. F) BS13-8, Spokane Formation, White Sulphur Springs. G) BS13-6, Spokane Formation, White Sulphur Springs. All except F were used for elemental abundance quantification in Table S5.4.

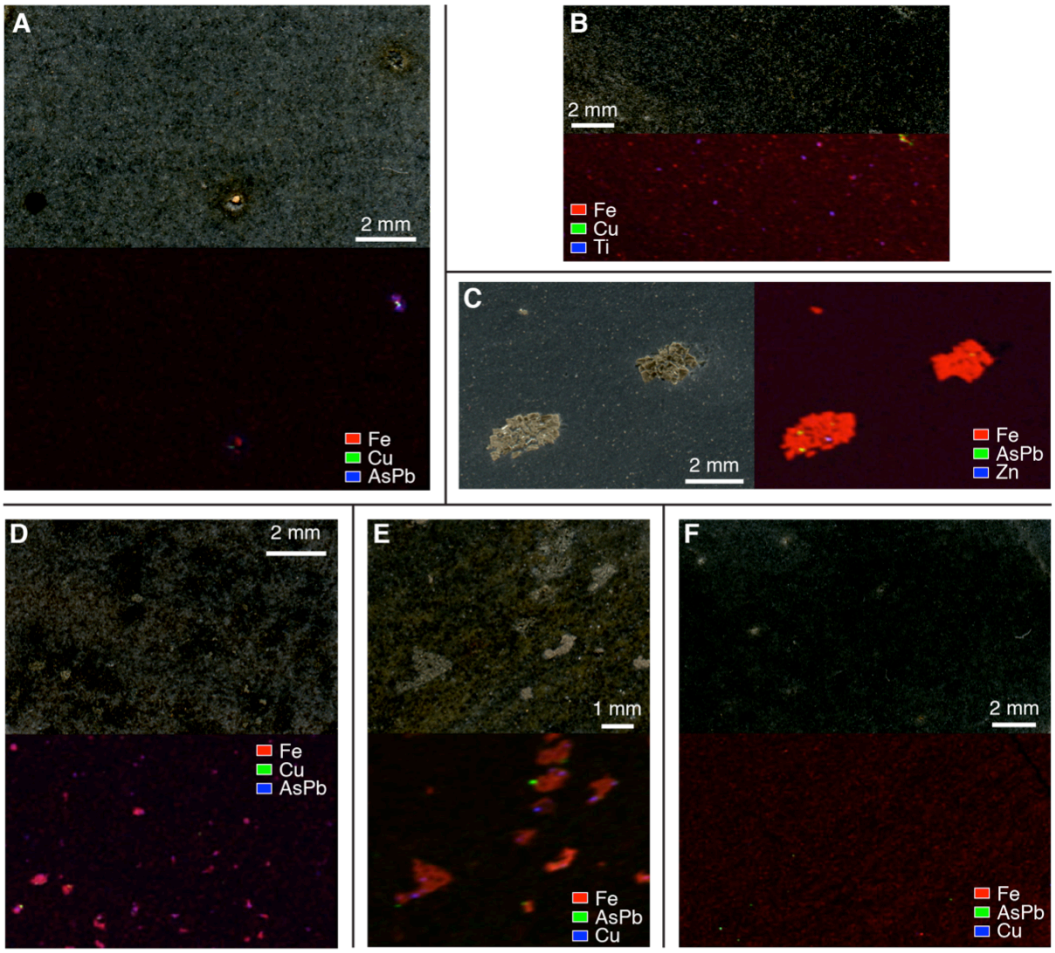

Figure S5.9: High-energy X-ray fluorescence (XRF) maps displaying elemental abundances paired with scans of the corresponding thick section region in the Prichard Formation. Separate scale bar and element key for each image pair (black to brightly colored at maximum). A) BS13-37, Transition Member, Libby. B) BS13-31, Unit C Hope. C) BS13-29, Unit F, Sagle Point. D) PP13-13, Unit F, 171 m away from sill, Perma. E) PP13-11, Unit F, 25 m away from sill, Perma. F) PP13-6, Unit F, 1.6 m away from sill, Perma. All were used for elemental abundance quantification in Table S5.4.

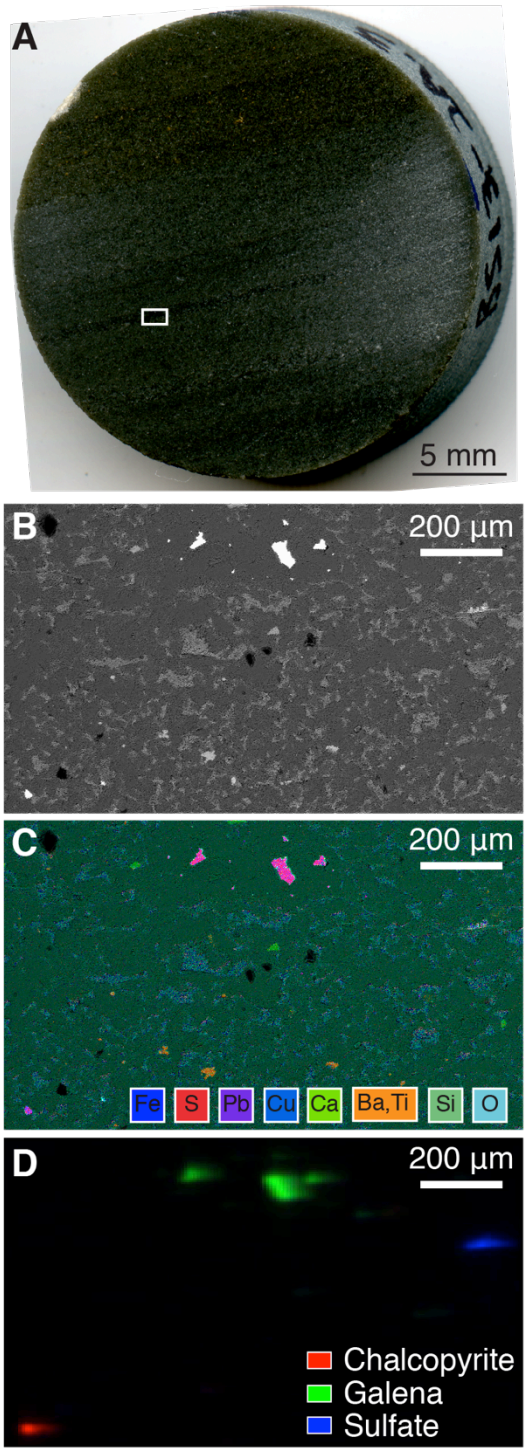

Figure S5.10: Detailed textural analysis of sample BS13-2, Lower Chamberlain Formation, White Sulphur Springs reveals euhedral base-metal sulfide grains

where the galena grains potentially formed from a larger recrystallized sulfide grain based on texture. Additionally, a recrystallized or secondary barite grain is found. A) Image of thick section with box showing region displayed in parts B-D. B) Backscatter electron image. C) Energy dispersive X-ray spectroscopy (EDS) map. E) Multiple energy X-ray fluorescence (XRF) map at sulfur energies fitted with end-member X-ray absorption near-edge spectra (XANES) shown in Figure S5.5.

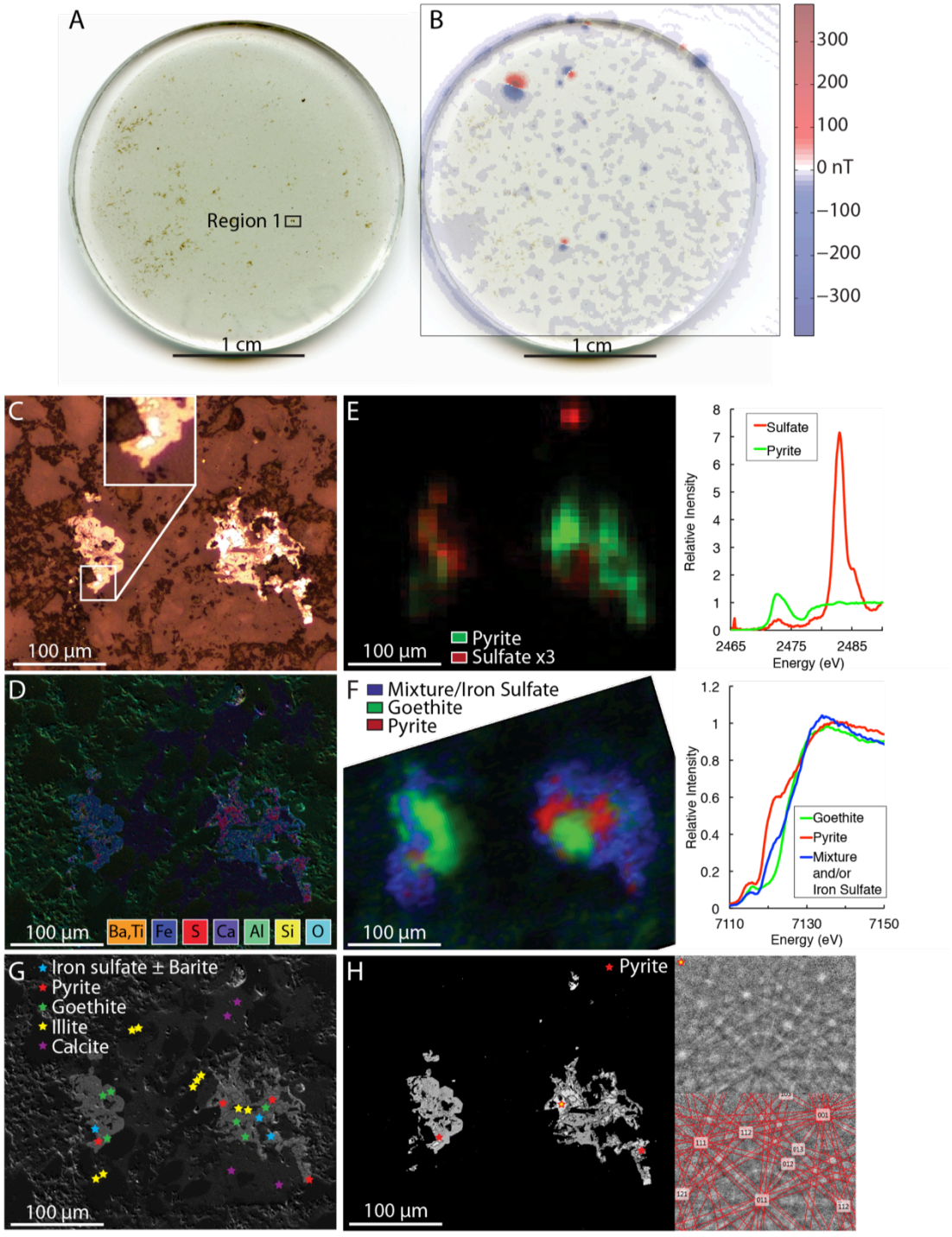

Figure S5.11: Detailed textural analysis of sample GP12-1, Appekunny Formation, Member 2, east side of Glacier National Park reveals scattered

background magnetic dipoles and pyrite surrounded by goethite, interpreted to be surface weathering replacement of euhedral recrystallized sulfide nodules. Iron sulfates and barite also occur in the goethite rim and barite occurs as separate grains, interpreted to be authigenic replacements (not detrital or water column) from post-depositional oxidizing fluids or more likely, diagenesis in pore fluids. A) Image of thin section. B) Ultrahigh resolution scanning SQuID microscope (UHRSSM) image. C) Reflected light microscopy with inset highlighting goethite rim around pyrite. D) Energy dispersive X-ray spectroscopy (EDS) map. E) Multiple energy X-ray fluorescence (XRF) map at sulfur energies fitted with displayed end-member X-ray absorption near-edge spectra (XANES). F) Multiple energy XRF map at iron energies fitted to displayed end-member XANES. G) Electron probe micro-analyzer (EPMA) point mineral identifications on backscatter electron image (see Table S5.3 for detailed formulas). H) Electron backscatter diffraction (EBSD) point mineral identifications on backscatter electron image with diffraction pattern and standard match of select point shown.

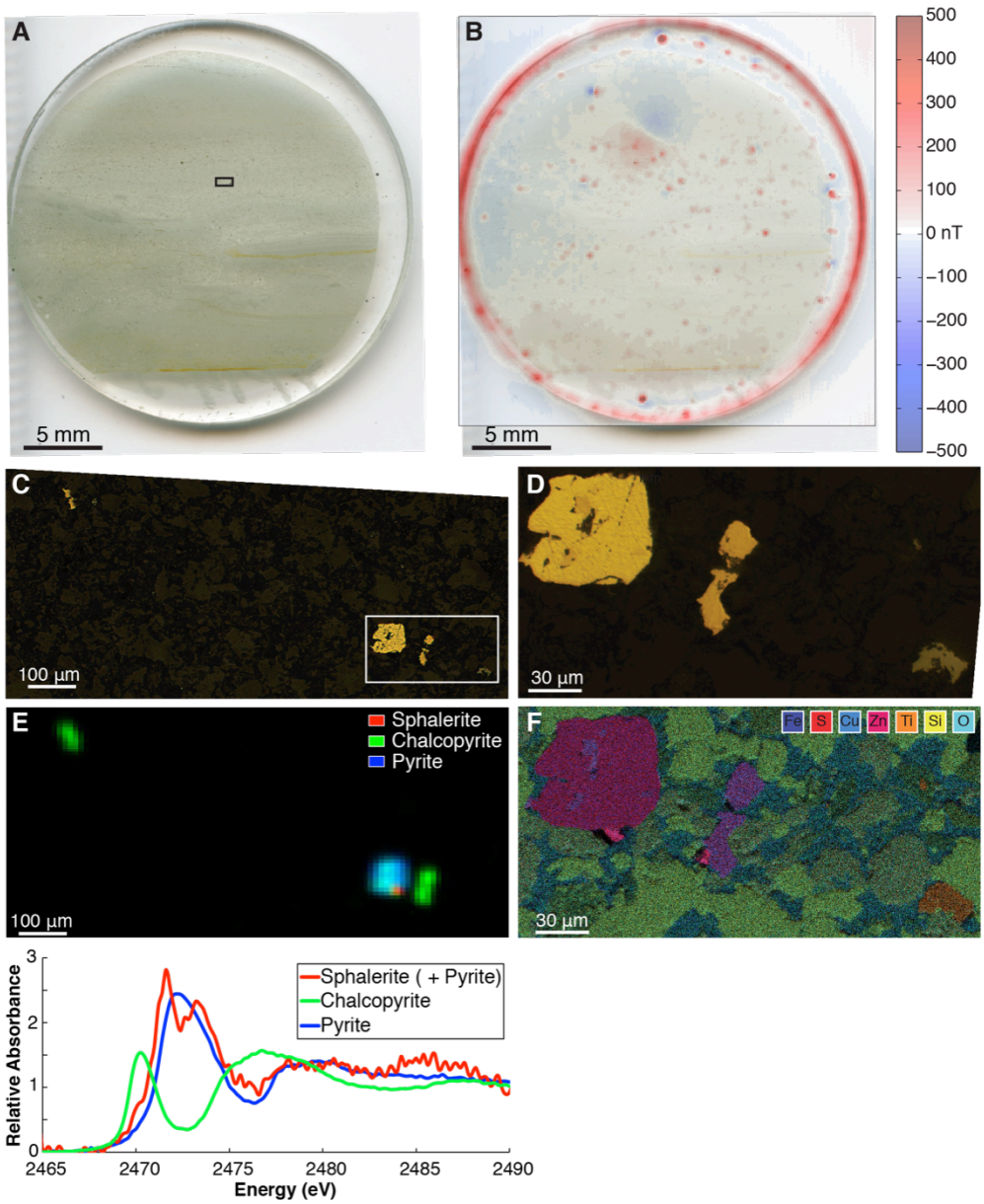

Figure S5.12: Detailed textural analysis of sample GP14-32, Appekunny Formation Member 5, east side of Glacier National Park reveals scattered background magnetic dipoles and euhedral sulfide nodules composed of multiple phases—pyrite, chalcopyrite, and sphalerite. A) Image of thin section with box showing region displayed in parts C and E. B) Ultrahigh resolution scanning SQuID microscope (UHRSSM) image. C) Reflected light microscopy with box showing region in parts D and F. D) Reflected light microscopy. E) Multiple energy X-ray fluorescence (XRF) map at sulfur energies fitted with displayed end-member X-ray absorption near-edge spectra (XANES). F) Energy dispersive X-ray spectroscopy (EDS) map.

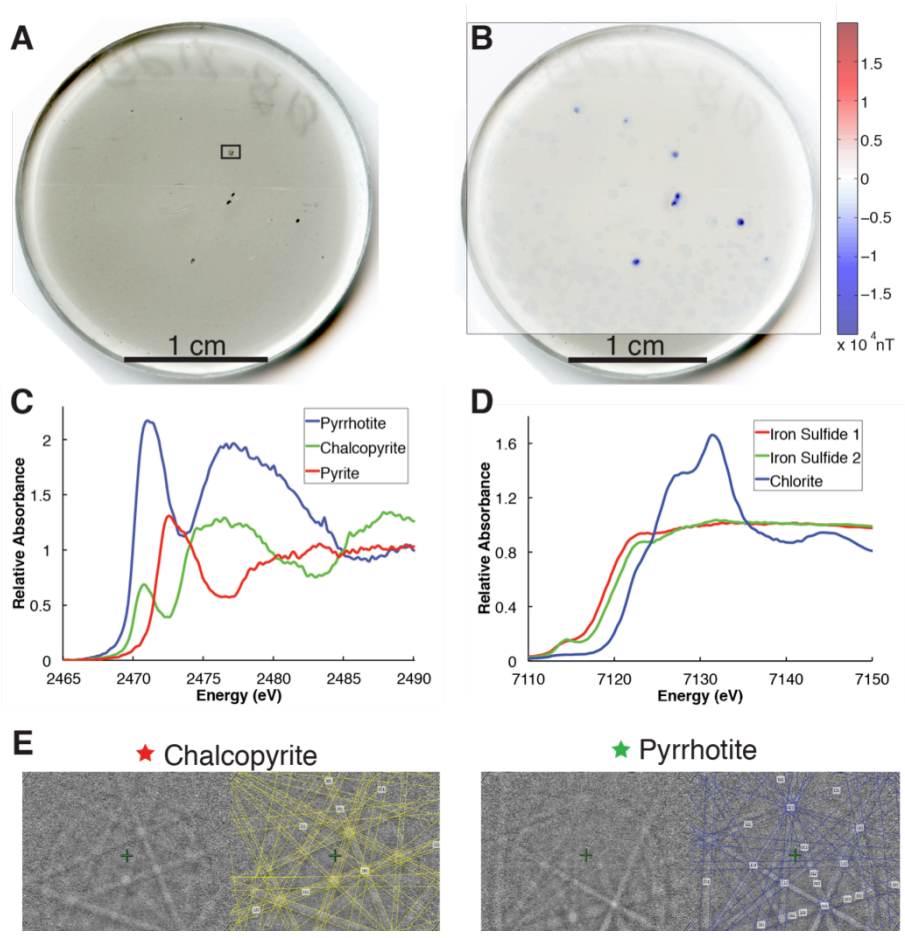

Figure S5.13: Additional textural analyses of sample GP12-8, Appekunny Formation Member 4 or Prichard Formation, west side of Glacier National Park highlight that the pyrrhotite nodules are magnetic. A) Image of thin section with box showing region displayed in Figure 5.4. B) Ultrahigh resolution scanning SQuID microscope (UHRSSM) image. C) End-member X-ray absorption near-edge spectra (XANES) at sulfur energies to which Figure 5.4C was fit. E) End-member XANES at iron energies to which Figure 5.4D was fit. E) Example electron backscatter diffraction (EBSD) patterns and standard match from the ones used to identify points shown in Figure 5.4E.

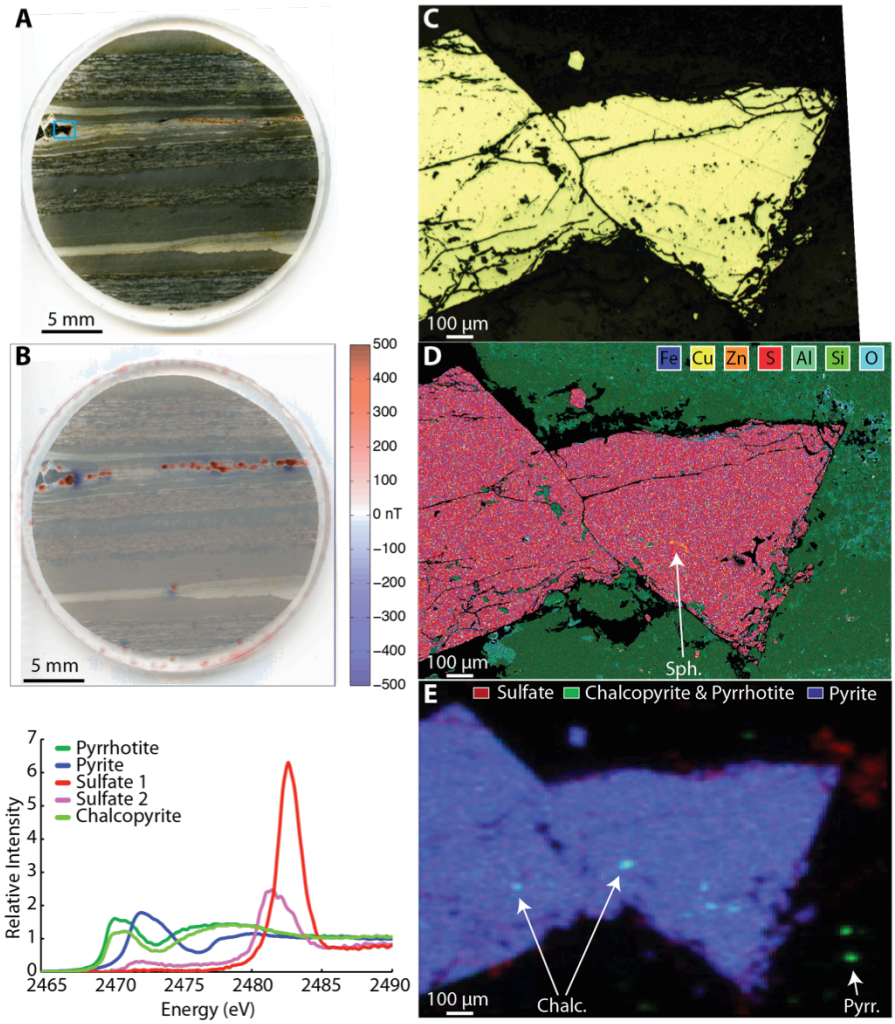

Figure S5.14: Detailed textural analysis of sample GP14-6, Appekunny Formation Member 4 or Prichard Formation, west side of Glacier National Park displays strong magnetic dipoles concentrated to certain laminae surrounding large secondary euhedral pyrite nodules which contain small domains of chalcopyrite and sphalerite. Pyrrhotite is located in small neighboring grains. A) Image of thin section with box showing region displayed in parts C-E. B) Ultrahigh resolution scanning SQuID microscope (UHRSSM) image. C) Reflected light microscopy. D) Energy dispersive X-ray spectroscopy (EDS) map. E) Multiple energy X-ray fluorescence (XRF) map at sulfur energies fitted with displayed end-member X-ray absorption near-edge spectra (XANES). Due to limitations in the mapping software, chalcopyrite and pyrrhotite are fit together even through the pyrrhotite spectra was used for analysis. Additional end-member XANES spectra are included for chalcopyrite and a second sulfate mineral to show their presence in the sample.

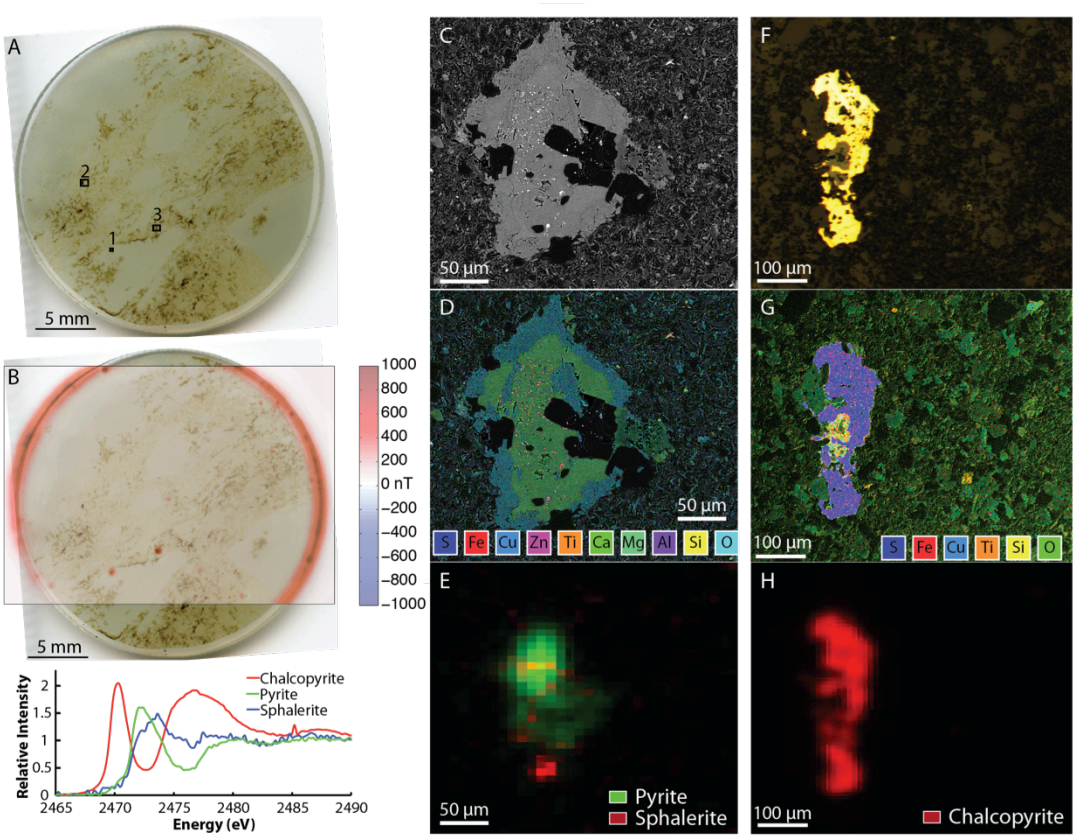

Figure S5.15: Detailed textural analysis of sample of GP14-27, Appekunny Formation Member 5, west side of Glacier National Park displays strong magnetic dipoles near recrystallized pyrite nodules suggesting the goethite detected in magnetic measurements is localized and from surface weathering. Sulfide minerals include chalcopyrite, sphalerite, and pyrite; chalcopyrite occurs in large distinct nodules while the sphalerite and pyrite are recrystallized remanents of a former nodule within a calcite and chlorite rim with neighboring Fe-rich dolomite. A) Image of thin section with boxes showing numbered regions displayed in parts C-E and parts F-H and in Figure 5.3D. B) Ultrahigh resolution scanning SQuID microscope (UHRSSM) image. C) Backscatter electron image of Region 1. D) Energy dispersive X-ray spectroscopy (EDS) map of Region 1. E) Multiple energy XRF map at sulfur energies of Region 1. F) Backscatter electron image of Region 2. G) EDS map of Region 2. H) Multiple energy X-ray fluorescence (XRF) map at sulfur energies of Region 2. E and H fitted with the same end-member X-ray absorption near-edge spectra (XANES) shown in Figure S5.5.

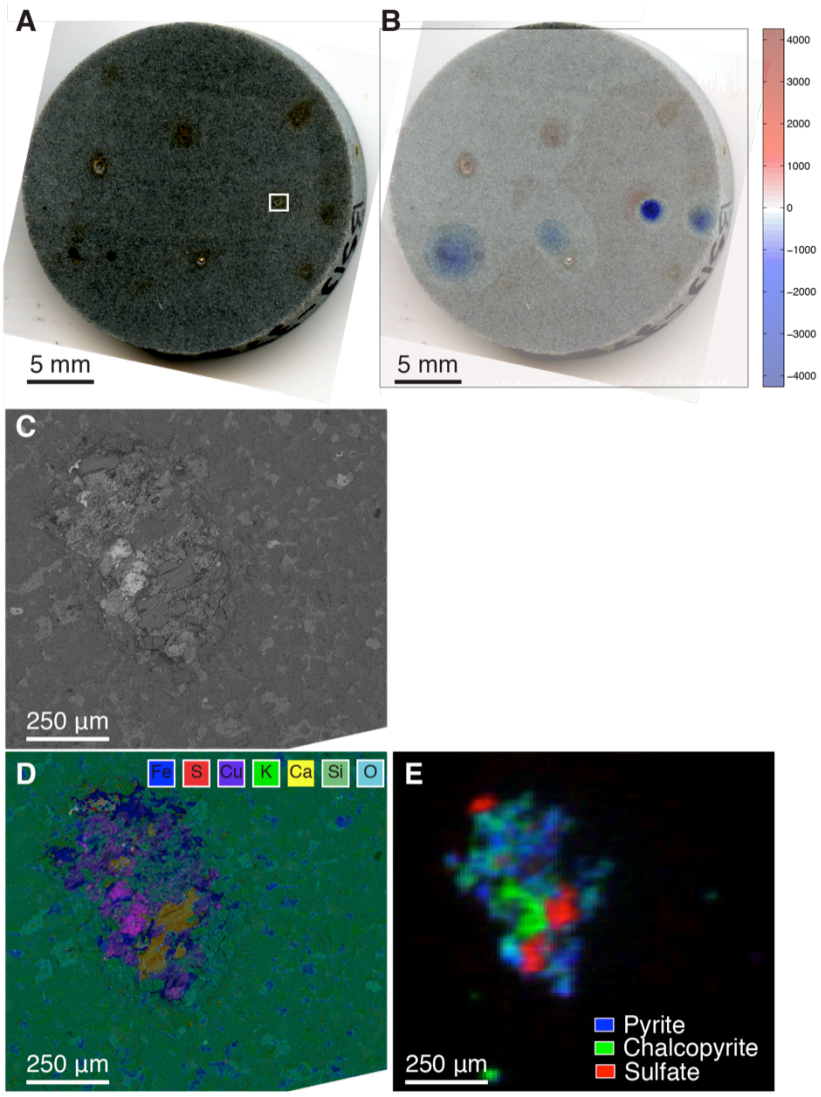

Figure S5.16: Detailed textural analysis of sample of BS13-37, Prichard Formation, Transition Member, Libby displays weathered pits from iron sulfides with mixed nodules of pyrite, chalcopyrite, and calcium sulfate remaining. Background magnetic dipoles are concentrated in near the pits and could be predominantly surface-weathering goethite identified using magnetic techniques. A) Image of thick section with boxes showing numbered regions displayed in parts C-E. B) Ultrahigh resolution scanning SQuID microscope (UHRSSM) image. C) Backscatter electron image. D) Energy dispersive X-ray spectroscopy (EDS) map. E) Multiple energy XRF map at sulfur energies fitted with the end-member X-ray absorption near-edge spectra (XANES) shown in Figure S5.5.

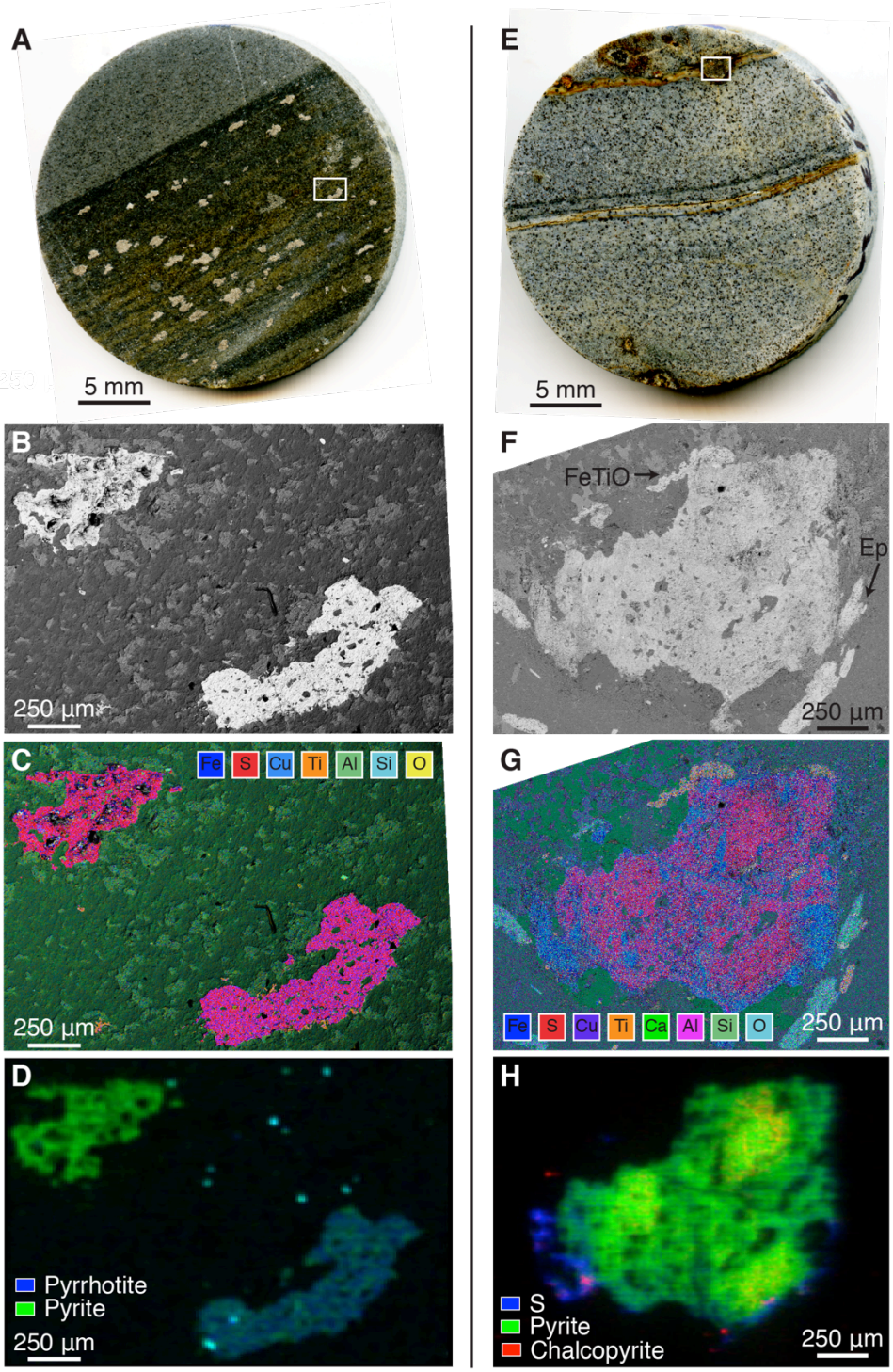

Figure S5.17: Detailed textural analysis of samples PP13-11 and BS13-39. Analyses of PP13-1, Prichard Formation, Unit F, 25m from sill, Perma reveal

large secondary pyrite and pyrrhotite nodules that contain small domains of chalcopyrite. A) Image of thick section with box showing region displayed in parts B-D. B) Backscatter electron image. C) Energy dispersive X-ray spectroscopy (EDS) map. D) Multiple energy X-ray fluorescence (XRF) map at sulfur energies fitted with end-member X-ray absorption near-edge spectra (XANES) shown in Figure S5.5. Analyses of BS13-39, Prichard Formation, Upper Member, Libby reveal a large secondary pyrite nodule with small domains of chalcopyrite rimmed by elemental sulfur and iron titanium oxides. Discrete grains of chalcopyrite are also present along with euhedral grains of iron titanium oxides and epidote. E) Image of thick section with box showing region displayed in parts F-G with example epidote (Ep) and the iron titantium oxide (FeTiO) grains identified with arrows. F) Backscatter electron image. G) EDS map. H) Multiple energy XRF map at sulfur energies fitted with end-member XANES shown in Figure S5.5.

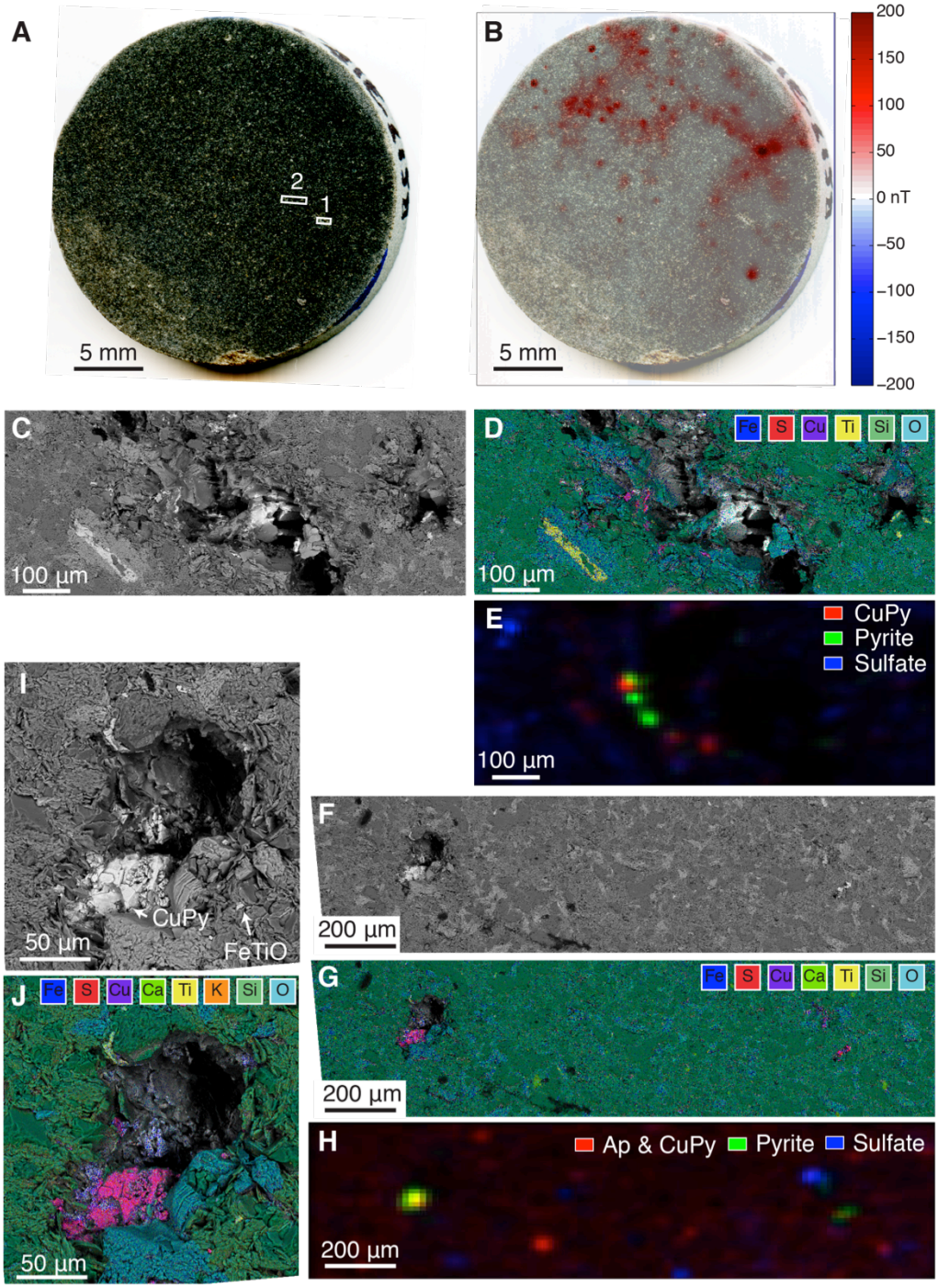

Figure S5.18: Detailed textural analysis of sample of BS13-31, Prichard Formation, Unit F, Hope displays weathered pits from iron sulfides with mixed nodules of pyrite, chalcocite, and chalcopyrite remaining. Iron titanium oxide

(FeTiO) occurs within this sample in small and large secondary euhedral grains; background magnetic dipoles appear concentrated in certain regions, but not specifically on weathered sulfide pits. A) Image of thick section with boxes showing numbered regions displayed in parts C-E and parts F-H. B) Ultrahigh resolution scanning SQuID microscope (UHRSSM) image. C) Backscatter electron image of Region 1. D) Energy dispersive X-ray spectroscopy (EDS) map of Region 1. E) Multiple energy XRF map at sulfur energies of Region 1. F) Backscatter electron image of Region 2. Based on EDS, the chalcopyrite (CuPy) may actually be chalcocite in this region. G) EDS map of Region 2. H) Multiple energy X-ray fluorescence (XRF) map at sulfur energies of Region 2. E and H fitted with the same end-member X-ray absorption near-edge spectra (XANES) shown in Figure S5.5; subtle differences in copper sulfides are based on EDS data. Note that apatite (Ap) is included with chalcopyrite (CuPy) on the XRF maps due to limitations of the fitting program. I) Zoomed backscatter electron image of sulfide nodule in Region 2 with chalcopyrite and FeTiO pointed out with arrows. J) Zoomed EDS of sulfide nodule in Region 2.

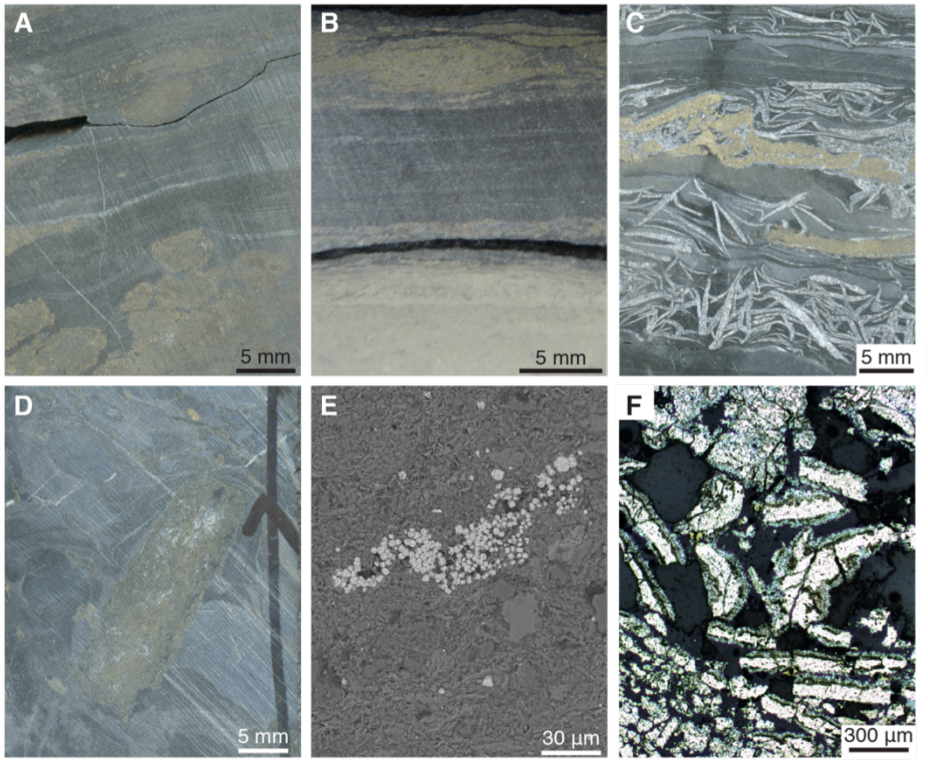

Figure S5.19. Macroscopic and microscopic textures in Newland Formation samples from the Black Butte Deposit drill core highlighting early diagenetic formation of pyrite and sulfates. A) SC11-095, 140.39 displays differential compaction of dolomitic shale layers around early pyrite nodules. B) SC11-09, 388.26 also shows differential compaction of dolomitic shale around early pyrite nodules and laminae. C) SC11-61.27 displays differential compaction of dolomitic shale laminae around early diagenetic barite laths with secondary intergrown sub-parallel iron sulfides. D) SC11-095, 400.83 displays a debris flow clast made of pyrite. E) The backscatter electron image of T095-53 (SC11-095, 53.52 m) shows it contains fine-grained recrystallized pyrite framboids. F) The reflected light image of T029-76 (SC11-029, 76.34 m) displays broken detrital early iron sulfide tubes.

5.12 References

Algoe, C., Stoops, G., Vandenberghe, R., and Van Ranst, E., 2012, Selective dissolution of Fe–Ti oxides—Extractable iron as a criterion for andic properties revisited: Catena, v. 92, p. 49-54.

Anderson, H. E., and Davis, D. W., 1995, U-Pb geochronology of the Moyie sills, Purcell Supergroup, southeastern British Columbia: implications for the Mesoproterozoic geological history of the Purcell (Belt) basin: Canadian Journal of Earth Sciences, v. 32, no. 8, p. 1180-1193.

Asael, D., Tissot, F. L., Reinhard, C. T., Rouxel, O., Dauphas, N., Lyons, T. W., Ponzevera, E., Liorzou, C., and Chéron, S., 2013, Coupled molybdenum, iron and uranium stable isotopes as oceanic paleoredox proxies during the Paleoproterozoic Shunga Event: Chemical Geology, v. 362, p. 193-210.

Aubourg, C., and Pozzi, J.-P., 2010, Toward a new< 250 C pyrrhotite–magnetite geothermometer for claystones: Earth and Planetary Science Letters, v. 294, no. 1, p. 47-57.

Berkner, L., and Mashall, L., 1964, The History of Growth of Oxygen in the Earth's Atmosphere, *in* Brancazio, P., and Cameron, A., eds., The Origin and Evolution of Atmospheres and Oceans: New York, John WIley & Sons, Inc.

Berner, R. A., 1984, Sedimentary pyrite formation: an update: Geochimica et Cosmochimica Acta, v. 48, no. 4, p. 605-615.

Besnus, M., and Meyer, A., Nouvelles données expérimentales sur le magnétisme de la pyrrhotine naturelle, *in* Proceedings Proc. Int. Conf. Mag., Nottingham1964, Volume 20, p. 507-511.

Bishop, D., 1972, Progressive metamorphism from prehnite-pumpellyite to greenschist facies in the Dansey Pass area, Otago, New Zealand: Geological Society of America Bulletin, v. 83, no. 11, p. 3177-3198.

Burton, E. D., Bush, R. T., and Sullivan, L. A., 2006, Sedimentary iron geochemistry in acidic waterways associated with coastal lowland acid sulfate soils: Geochimica et Cosmochimica Acta, v. 70, no. 22, p. 5455-5468.

Canfield, D. E., and Berner, R. A., 1987, Dissolution and pyritization of magnetite in anoxie marine sediments: Geochimica et Cosmochimica Acta, v. 51, no. 3, p. 645-659.

Clarkson, M., Poulton, S., Guilbaud, R., and Wood, R., 2014, Assessing the utility of Fe/Al and Fe-speciation to record water column redox conditions in carbonate-rich sediments: Chemical Geology, v. 382, p. 111-122.

Cloud, P. E., 1968, Atmospheric and Hydrospheric Evolution on the Primitive Earth: Science, v. 160, no. 3829, p. 729-736.

Craig, J. R., and Vokes, F. M., 1993, The metamorphism of pyrite and pyritic ores: an overview: Mineralogical Magazine, v. 57, no. 1, p. 3-18.

Cressman, E. R., 1989, Reconnaissance stratigraphy of the Prichard Formation (Middle Proterozoic) and the early development of the Belt Basin, Washington, Idaho, and Montana: United States Geological Survey, Professional Paper, v. 1490, p. 80.

Crowe, S. A., Paris, G., Katsev, S., Jones, C., Kim, S.-T., Zerkle, A. L., Nomosatryo, S., Fowle, D. A., Adkins, J. F., and Sessions, A. L., 2014, Sulfate was a trace constituent of Archean seawater: Science, v. 346, no. 6210, p. 735-739.

Day, R., Fuller, M., and Schmidt, V., 1977, Hysteresis properties of titanomagnetites: grain-size and compositional dependence: Physics of the Earth and Planetary Interiors, v. 13, no. 4, p. 260-267.

Duke, E. F., and Lewis, R. S., 2010, Near infrared spectra of white mica in the Belt Supergroup and implications for metamorphism: American Mineralogist, v. 95, no. 7, p. 908-920.

Dunlop, D. J., 2002, Theory and application of the Day plot (Mrs/Ms versus Hcr/Hc) 1. Theoretical curves and tests using titanomagnetite data: Journal of Geophysical Research: Solid Earth, v. 107, no. B3, p. EPM 4-1-EPM 4-22.

Embley, T. M., and Martin, W., 2006, Eukaryotic evolution, changes and challenges: Nature, v. 440, no. 7084, p. 623-630.

Evans, K. V., Aleinikoff, J. N., Obradovich, J. D., and Fanning, C. M., 2000, SHRIMP U-Pb geochronology of volcanic rocks, Belt Supergroup, western Montana: evidence for rapid deposition of sedimentary strata: Canadian Journal of Earth Sciences, v. 37, no. 9, p. 1287-1300.

Ferry, J. M., 1983, Regional metamorphism of the Vassalboro Formation, south-central Maine, USA: a case study of the role of fluid in metamorphic petrogenesis: Journal of the Geological Society, v. 140, no. 4, p. 551-576.

-, 1984, A biotite isograd in south-central Maine, USA: mineral reactions, fluid transfer, and heat transfer: Journal of Petrology, v. 25, no. 4, p. 871-893.

-, 1988, Infiltration-driven metamorphism in northern New England, USA: Journal of Petrology, v. 29, no. 6, p. 1121-1159.

-, 2007, The role of volatile transport by diffusion and dispersion in driving biotite-forming reactions during regional metamorphism of the Gile Mountain Formation, Vermont: American Mineralogist, v. 92, no. 8-9, p. 1288-1302.

Fischer, W. W., 2016, Breathing room for early animals: Proceedings of the National Academy of Sciences, v. 113, no. 7, p. 1686-1688.

Fleet, M. E., 2005, XANES spectroscopy of sulfur in earth materials: The Canadian Mineralogist, v. 43, no. 6, p. 1811-1838.

French, B. M., 1973, Mineral assemblages in diagenetic and low-grade metamorphic iron-formation: Economic Geology, v. 68, no. 7, p. 1063-1074.

Fuller, M., Cisowski, S., Hart, M., Haston, R., Schmidtke, E., and Jarrard, R., 1988, NRM-IRM(s) Demagnetization Plots - an Aid to the Interpretation of Natural Remanent Magnetization: Geophysical Research Letters, v. 15, no. 5, p. 518-521.

Fuller, M., Kidane, T., and Ali, J., 2002, AF demagnetization characteristics of NRM, compared with anhysteretic and saturation isothermal remanence: an aid in the interpretation of NRM: Physics and Chemistry of the Earth, v. 27, no. 25-31, p. 1169-1177.

Gellatly, A. M., and Lyons, T. W., 2005, Trace sulfate in mid-Proterozoic carbonates and the sulfur isotope record of biospheric evolution: Geochimica et Cosmochimica Acta, v. 69, no. 15, p. 3813-3829.

Gilleaudeau, G. J., and Kah, L. C., 2015, Heterogeneous redox conditions and a shallow chemocline in the Mesoproterozoic ocean: evidence from carbon–sulfur–iron relationships: Precambrian Research, v. 257, p. 94-108.

González-Álvarez, I., and Kerrich, R., 2010, REE and HFSE mobility due to protracted flow of basinal brines in the Mesoproterozoic Belt-Purcell Supergroup, Laurentia: Precambrian Research, v. 177, no. 3, p. 291-307.

González-Álvarez, I., Kusiak, M. A., and Kerrich, R., 2006, A trace element and chemical Th–U total Pb dating study in the lower Belt-Purcell Supergroup,

Western North America: provenance and diagenetic implications: Chemical Geology, v. 230, no. 1, p. 140-160.

Graham, G., Hitzman, M. W., and Zieg, J., 2012, Geologic Setting, Sedimentary Architecture, and Paragenesis of the Mesoproterozoic Sediment-Hosted Sheep Creek Cu-Co-Ag Deposit, Helena Embayment, Montana: Economic Geology, v. 107, no. 6, p. 1115-1141.

Grotzinger, J. P., 1981, The stratigraphy and sedimentation of the Wallace Formation northwest Montana and northern Idaho [M.S. Thesis: University of Montana, 153 p.

Halevy, I., 2013, Production, preservation, and biological processing of mass-independent sulfur isotope fractionation in the Archean surface environment: Proceedings of the National Academy of Sciences, v. 110, no. 44, p. 17644-17649.

Hall, A. J., 1986, Pyrite-pyrrhotine redox reactions in nature: Mineralogical Magazine, v. 50, p. 223-229.

Hamilton, J., Bishop, D., Morris, H., and Owens, O., 1982, Geology of the Sullivan orebody, Kimberley, BC, Canada: Precambrian Sulphide Deposits, v. 25, p. 597-665.

Hansel, C. M., Lentini, C. J., Tang, Y., Johnston, D. T., Wankel, S. D., and Jardine, P. M., 2015, Dominance of sulfur-fueled iron oxide reduction in low-sulfate freshwater sediments: The ISME Journal, v. 9, no. 11, p. 2400-2412.

Harrison, J. E., 1972, Precambrian Belt basin of northwestern United States: Its geometry, sedimentation, and copper occurrences: Geological Society of America Bulletin, v. 83, no. 5, p. 1215-1240.

Heslop, D., Dekkers, M., Kruiver, P., and Van Oorschot, I., 2002, Analysis of isothermal remanent magnetization acquisition curves using the expectation-maximization algorithm: Geophysical Journal International, v. 148, no. 1, p. 58-64.

Hilscher, G., Peter, R., Zemann, J., and Ntaflos, T., 2005, Low-temperature magnetic investigation of ankerite: European journal of mineralogy, v. 17, no. 1, p. 103-105.

Holland, H. D., 1984, The chemical evolution of the atmosphere and oceans, Princeton University Press.

Horng, C.-S., and Roberts, A. P., 2006, Authigenic or detrital origin of pyrrhotite in sediments?: Resolving a paleomagnetic conundrum: Earth and Planetary Science Letters, v. 241, no. 3, p. 750-762.

Horodyski, R. J., Winston, D., and Whipple, J. W., 1989, Paleontology of the middle Proterozoic belt supergroup, *in* Winston, D., Horodyski, R. J., and Whipple, J. W., eds., Middle Proterozoic Belt Supergroup, Western Montana: Great Falls, Montana to Spokane, Washington: 28th International Geological Congress, Field Trip Guidebook T334, p. 7-26.

Housen, B. A., Banerjee, S., and Moskowitz, B., 1996, Low‐temperature magnetic properties of siderite and magnetite in marine sediments: Geophysical Research Letters, v. 23, no. 20, p. 2843-2846.

Huebschman, R. P., 1973, Correlation of fine carbonaceous bands across a Precambrian stagnant basin: Journal of Sedimentary Research, v. 43, no. 3, p. 688-699.

Kendall, B., Creaser, R. A., Gordon, G. W., and Anbar, A. D., 2009, Re–Os and Mo isotope systematics of black shales from the Middle Proterozoic Velkerri and Wollogorang formations, McArthur Basin, northern Australia: Geochimica et Cosmochimica Acta, v. 73, no. 9, p. 2534-2558.

Kholodov, V., and Butuzova, G. Y., 2008, Siderite formation and evolution of sedimentary iron ore deposition in the Earth's history: Geology of Ore Deposits, v. 50, no. 4, p. 299-319.

Kirschvink, J. L., Kopp, R. E., Raub, T. D., Baumgartner, C. T., and Holt, J. W., 2008, Rapid, precise, and high-sensitivity acquisition of paleomagnetic and rock-magnetic data: Development of a low-noise automatic sample changing system for superconducting rock magnetometers: Geochemistry Geophysics Geosystems, v. 9, no. 5.

Klein, F., Bach, W., Humphris, S. E., Kahl, W.-A., Jöns, N., Moskowitz, B., and Berquó, T. S., 2014, Magnetite in seafloor serpentinite—Some like it hot: Geology, v. 42, no. 2, p. 135-138.

Knoll, A. H., Javaux, E. J., Hewitt, D., and Cohen, P., 2006, Eukaryotic organisms in Proterozoic oceans: Philosophical Transactions of the Royal Society B: Biological Sciences, v. 361, no. 1470, p. 1023-1038.

Koeksoy, E., Halama, M., Konhauser, K. O., and Kappler, A., 2015, Using modern ferruginous habitats to interpret Precambrian banded iron formation deposition: International Journal of Astrobiology, p. 1-13.

Larrasoaña, J. C., Roberts, A. P., Musgrave, R. J., Gràcia, E., Piñero, E., Vega, M., and Martínez-Ruiz, F., 2007, Diagenetic formation of greigite and pyrrhotite in gas hydrate marine sedimentary systems: Earth and Planetary Science Letters, v. 261, no. 3, p. 350-366.

Lentini, C. J., Wankel, S. D., and Hansel, C., 2012, Enriched iron (III)-reducing bacterial communities are shaped by carbon substrate and iron oxide mineralogy: Frontiers in Microbiology, v. 3, p. 404.

Li, C., Planavsky, N. J., Love, G. D., Reinhard, C. T., Hardisty, D., Feng, L., Bates, S. M., Huang, J., Zhang, Q., and Chu, X., 2015, Marine redox conditions in the middle Proterozoic ocean and isotopic constraints on authigenic carbonate formation: Insights from the Chuanlinggou Formation, Yanshan Basin, North China: Geochimica et Cosmochimica Acta, v. 150, p. 90-105.

Liu, Q., Yu, Y., Torrent, J., Roberts, A. P., Pan, Y., and Zhu, R., 2006, Characteristic low‐temperature magnetic properties of aluminous goethite [α‐(Fe, Al) OOH] explained: Journal of Geophysical Research: Solid Earth, v. 111, no. B12.

Luepke, J. J., and Lyons, T. W., 2001, Pre-Rodinian (Mesoproterozoic) supercontinental rifting along the western margin of Laurentia: geochemical evidence from the Belt-Purcell Supergroup: Precambrian Research, v. 111, no. 1, p. 79-90.

Lyons, T. W., Luepke, J. J., Schreiber, M. E., and Zieg, G. A., 2000, Sulfur geochemical constraints on Mesoproterozoic restricted marine deposition: lower Belt Supergroup, northwestern United States: Geochimica et Cosmochimica Acta, v. 64, no. 3, p. 427-437.

Lyons, T. W., and Severmann, S., 2006, A critical look at iron paleoredox proxies: new insights from modern euxinic marine basins: Geochimica et Cosmochimica Acta, v. 70, no. 23, p. 5698-5722.

Mayhew, L., Webb, S., and Templeton, A., 2011, Microscale imaging and identification of Fe speciation and distribution during fluid–mineral reactions under highly reducing conditions: Environmental science & technology, v. 45, no. 10, p. 4468-4474.

Moreau, M., Ader, M., and Enkin, R., 2005, The magnetization of clay-rich rocks in sedimentary basins: low-temperature experimental formation of magnetic carriers in natural samples: Earth and Planetary Science Letters, v. 230, no. 1, p. 193-210.

Muffler, L. P., and White, D. E., 1969, Active metamorphism of upper Cenozoic sediments in the Salton Sea geothermal field and the Salton Trough, southeastern California: Geological Society of America Bulletin, v. 80, no. 2, p. 157-182.

Nadoll, P., Mauk, J. L., Hayes, T. S., Koenig, A. E., and Box, S. E., 2012, Geochemistry of magnetite from hydrothermal ore deposits and host rocks of the Mesoproterozoic Belt Supergroup, United States: Economic Geology, v. 107, no. 6, p. 1275-1292.

O'Day, P. A., Rivera, N., Root, R., and Carroll, S. A., 2004, X-ray absorption spectroscopic study of Fe reference compounds for the analysis of natural sediments: American Mineralogist, v. 89, no. 4, p. 572-585.

Partin, C., Bekker, A., Planavsky, N., and Lyons, T., 2015, Euxinic conditions recorded in the ca. 1.93 Ga Bravo Lake Formation, Nunavut (Canada): Implications for oceanic redox evolution: Chemical Geology, v. 417, p. 148-162.

Peters, C., and Dekkers, M., 2003, Selected room temperature magnetic parameters as a function of mineralogy, concentration and grain size: Physics and Chemistry of the Earth, v. 28, no. 16, p. 659-667.

Piché, M., and Jébrak, M., 2006, Determination of alteration facies using the normative mineral alteration index: Selbaie Cu-Zn deposit, northern Abitibi greenstone belt, Canada: Canadian Journal of Earth Sciences, v. 43, no. 12, p. 1877-1885.

Planavsky, N. J., McGoldrick, P., Scott, C. T., Li, C., Reinhard, C. T., Kelly, A. E., Chu, X., Bekker, A., Love, G. D., and Lyons, T. W., 2011, Widespread iron-rich conditions in the mid-Proterozoic ocean: Nature, v. 477, no. 7365, p. 448-451.

Potter, D., and Stephenson, A., 1986, The detection of fine particles of magnetite using anhysteretic and rotational remanent magnetizations: Geophysical Journal International, v. 87, no. 2, p. 569-582.

Poulton, S. W., and Canfield, D. E., 2005, Development of a sequential extraction procedure for iron: implications for iron partitioning in continentally derived particulates: Chemical Geology, v. 214, no. 3, p. 209-221.

-, 2011, Ferruginous conditions: a dominant feature of the ocean through Earth's history: Elements, v. 7, no. 2, p. 107-112.

Present, T. M., Bergmann, K. D., Meyers, C. E., Slotznick, S. P., Creveling, J. R., Zieg, G. A., Fischer, W. W., Knoll, A. H., and Grotzinger, J. P., in review, Pyrite-

walled tube structures in a Mesoproterozoic SEDEX massive sulfide deposit: Geological Society of America Bulletin.

Raiswell, R., Reinhard, C. T., Derkowski, A., Owens, J., Bottrell, S. H., Anbar, A. D., and Lyons, T. W., 2011, Formation of syngenetic and early diagenetic iron minerals in the late Archean Mt. McRae Shale, Hamersley Basin, Australia: New insights on the patterns, controls and paleoenvironmental implications of authigenic mineral formation: Geochimica et Cosmochimica Acta, v. 75, no. 4, p. 1072-1087.

Raub, T., Johnson, S. C., and Raub, T. D., 2012, Rock magnetic detection of the pyrite-to-pyrrhotite reduction: applications to hydrocarbon maturity, mineral resources, and biogeochemistry, American Geophysical Union, Fall Meeting: San Francisco, CA, p. GP34A-08.

Reinhard, C. T., Lyons, T. W., Rouxel, O., Asael, D., Dauphas, N., and Kump, L. R., 2013, 7.10.4 Iron Speciaiton and Isotope Perspectives on Palaeoproterozoic Water Column Chemistry, *in* Melezhik, V., Prave, A.R., Hanski, E.J., Fallick, A.E., Lepland, A., Kump, L.R., Strauss, H., ed., Reading the Archive of Earth's Oxygenation, Volume 3: Berlin Heidelberg, Springer, p. 1483-1492.

Reinhard, C. T., Raiswell, R., Scott, C., Anbar, A. D., and Lyons, T. W., 2009, A late Archean sulfidic sea stimulated by early oxidative weathering of the continents: Science, v. 326, no. 5953, p. 713-716.

Reuschel, M., Melezhik, V., and Strauss, H., 2012, Sulfur isotopic trends and iron speciation from the c. 2.0 Ga Pilgujärvi Sedimentary Formation, NW Russia: Precambrian Research, v. 196, p. 193-203.

Roberts, A. P., Liu, Q., Rowan, C. J., Chang, L., Carvallo, C., Torrent, J., and Horng, C. S., 2006, Characterization of hematite (α - Fe2O3), goethite (α - FeOOH), greigite (Fe3S4), and pyrrhotite (Fe7S8) using first - order reversal curve diagrams: Journal of Geophysical Research: Solid Earth, v. 111, no. B12.

Robertson, D., and France, D., 1994, Discrimination of remanence-carrying minerals in mixtures, using isothermal remanent magnetisation acquisition curves: Physics of the Earth and Planetary Interiors, v. 82, no. 3, p. 223-234.

Rochette, P., Fillion, G., Mattéi, J.-L., and Dekkers, M. J., 1990, Magnetic transition at 30–34 Kelvin in pyrrhotite: insight into a widespread occurrence of this mineral in rocks: Earth and Planetary Science Letters, v. 98, no. 3, p. 319-328.

Sears, J., Chamberlain, K., and Buckley, S., 1998, Structural and U-Pb geochronological evidence for 1.47 Ga rifting in the Belt basin, western Montana: Canadian Journal of Earth Sciences, v. 35, no. 4, p. 467-475.

Shen, Y., Knoll, A. H., and Walter, M. R., 2003, Evidence for low sulphate and anoxia in a mid-Proterozoic marine basin: Nature, v. 423, no. 6940, p. 632-635.

Skomurski, F. N., Kerisit, S., and Rosso, K. M., 2010, Structure, charge distribution, and electron hopping dynamics in magnetite (Fe 3 O 4)(100) surfaces from first principles: Geochimica et Cosmochimica Acta, v. 74, no. 15, p. 4234-4248.

Slotznick, S. P., Winston, D., Webb, S. M., Kirschvink, J. L., and Fischer, W. W., 2016, Iron mineralogy and redox conditions during deposition of the Mid-Proterozoic Appekunny Formation, Belt Supergroup, Glacier National Park: Geological Society of America Special Papers, v. 522.

Slotznick, S. P., Zieg, J., Webb, S. M., Kirschvink, J. L., and Fischer, W. W., 2015, Iron Mineralogy and Redox Chemistry of the Mesoproterozoic Newland Formation in the Helena Embayment, Belt Supergroup, Montana: Northwest Geology, v. 44, p. 55-72.

Snowball, I. F., 1997, The detection of single-domain greigite (Fe3S4) using rotational remanent magnetization (RRM) and the effective gyro field (Bg): mineral magnetic and palaeomagnetic applications: Geophysical Journal International, v. 130, no. 3, p. 704-716.

Sperling, E., Rooney, A., Hays, L., Sergeev, V., Vorob'eva, N., Sergeeva, N., Selby, D., Johnston, D., and Knoll, A., 2014, Redox heterogeneity of subsurface waters in the Mesoproterozoic ocean: Geobiology, v. 12, no. 5, p. 373-386.

Stüeken, E. E., 2013, A test of the nitrogen-limitation hypothesis for retarded eukaryote radiation: nitrogen isotopes across a Mesoproterozoic basinal profile: Geochimica et Cosmochimica Acta, v. 120, p. 121-139.

Summons, R. E., Bradley, A. S., Jahnke, L. L., and Waldbauer, J. R., 2006, Steroids, triterpenoids and molecular oxygen: Philosophical Transactions of the Royal Society B: Biological Sciences, v. 361, no. 1470, p. 951-968.

Suzuki, Y., Kopp, R. E., Kogure, T., Suga, A., Takai, K., Tsuchida, S., Ozaki, N., Endo, K., Hashimoto, J., and Kato, Y., 2006, Sclerite formation in the hydrothermal-vent “scaly-foot” gastropod—possible control of iron sulfide biomineralization by the animal: Earth and Planetary Science Letters, v. 242, no. 1, p. 39-50.

Tauxe, L., Mullender, T., and Pick, T., 1996, Potbellies, wasp-waists, and superparamagnetism in magnetic hysteresis: Journal of geophysical research, v. 101, p. 571-583.

Thomson, G. F., 1990, The anomalous demagnetization of pyrrhotite: Geophysical Journal International, v. 103, no. 2, p. 425-430.

Verwey, E., 1939, Electronic conduction of magnetite (Fe3O4) and its transition point at low temperatures: Nature, v. 144, no. 3642, p. 327-328.

Walker, J. C., and Brimblecombe, P., 1985, Iron and sulfur in the pre-biologic ocean: Precambrian Research, v. 28, no. 3-4, p. 205-222.

Webb, S. M., 2005, SIXPACK: A graphical user itnerface to XAS analysis using IFEFFIT: Physica Scripta, v. T115, p. 1011-1014.

-, 2011, The MicroAnalysis Toolkit: X-ray Fluorescence image processing software: AIP Conference Proceedings, v. 1365, p. 196-199.

Wilkin, R., and Barnes, H., 1997, Formation processes of framboidal pyrite: Geochimica et Cosmochimica Acta, v. 61, no. 2, p. 323-339.

Wilkin, R., Barnes, H., and Brantley, S., 1996, The size distribution of framboidal pyrite in modern sediments: an indicator of redox conditions: Geochimica et Cosmochimica Acta, v. 60, no. 20, p. 3897-3912.

Winston, D., 1986, Sedimentation and Tectonics of the Middle Proterozoic Belt Basin and Their Influence on Phanerozoic Compression and Extension in Western Montana and Northern Idaho: Part II. Northern Rocky Mountains, *in* Peterson, J. A., ed., Paleotectonics and sedimentation in the Rocky Mountain region, United States. American Association of Petroleum Geologists, Memoir 41, p. 87-118.

-, 2007, Revised Stratigraphy and Depositional History of the Helena and Wallace Formations, Mid-Proterozoic Piegan Group, Belt Supergroup Montana and Idaho: Special Publication-SEPM, v. 86, p. 65.

Winston, D., and Link, P., 1993, Middle Proterozoic rocks of Montana, Idaho and eastern Washington: the Belt Supergroup: Precambrian: Conterminous US: The Geology of North America, v. 2, p. 487-517.

Zieg, G., Scartozzi, V., Chutas, N., Albers, D., Gostomski, K., and Jones, J., 2013, Black Butte copper deposits, lower Belt Supergroup, Montana: Northwest Geology, v. 42, p. 131-147.